An Earth Image Simulation and Tracking System for the Mars Laser Communication Demonstration

by

Stephanie Karen Balster
Bachelor of Science, Electrical Science and Engineering

Submitted to the Department of Electrical Engineering and Computer Science

in partial fulfillment of the requirements for the degree of

Master of Engineering in Electrical Engineering and Computer Science

at the Massachusetts Institute of Technology

May 5, 2005

Author _____
Department of Electrical Engineering and Computer Science
May 4, 2005

Certified by _____
Frederick K. Knight
VI-A Company Thesis Supervisor

Certified by _____
Dennis M. Freeman
M.I.T. Thesis Supervisor

Accepted by _____
Arthur C. Smith
Chairman, Department Committee on Graduate Theses

This report is based on studies performed at Lincoln Laboratory, a center of research operated by the Massachusetts Institute of Technology. This work was sponsored by the National Aeronautics and Space Administration under Air Force Contract FA8721-05-C-0002. Opinions, interpretations, conclusions, and recommendations are those of the author and not necessarily endorsed by the United States Government.

An Earth Image Simulation and Tracking System for the Mars Laser Communication Demonstration

by

Stephanie Karen Balster

Submitted to the Department of Electrical Engineering and Computer Science
on May 5, 2005, in partial fulfillment of the
requirements for the degree of
Master of Engineering in Electrical Engineering and Computer Science

Abstract

In this thesis I created an Earth-image simulation and investigated Earth-tracking algorithms for the Mars Laser Communication Demonstration (MLCD). The MLCD mission will demonstrate the feasibility of high-data-rate laser communications between a Mars orbiting satellite and an Earth ground station. One of the key challenges of the mission is the requirement to achieve 0.35-μrad-accuracy pointing and tracking of the laser beam to maintain the 1-30 Mbps communication downlink from Mars to Earth. The sunlit Earth is a bright source and, for most of the mission, can be tracked to stabilize the telescope from disturbances between 0.02 to 2 Hz, while other stabilization systems will cover the rest of the frequency spectrum. Before testing candidate Earth-tracking algorithms, simulated Earth image sequences were created to provide test data sets. While a plain centroiding algorithm, thresholded-centroiding algorithm, cross-spectrum phase correlation method, and optical flow algorithm were all tested under various Earth phase conditions and pixel resolutions to evaluate their performance on simulated test data, the thresholded-centroiding algorithm was eventually chosen for its accuracy and low computational cost. The effect of short-term albedo variations on the performance of the thresholded-centroiding algorithm was shown to be limited by the Earth's rotation and too slow to change the Earth's surface enough to affect the centroid calculation between time frames. Differences between the geometric centroid and optical centroid were measured to be up to 10% of the Earth's diameter, or up to 2 focal plane array pixels during the mission at closest range. As such, the uncertainty area in which to search for the beacon at the ground receiving station is limited to a 2-pixel radius.

VI-A Company Thesis Supervisor: Frederick K. Knight
Title: Senior Staff, M.I.T. Lincoln Laboratory

M.I.T. Thesis Supervisor: Dennis M. Freeman
Title: Associate Professor

Acknowledgments

I would like to thank my supervisor, Fred Knight, for all his guidance and support in my work on this thesis. Thank you to Bill Ross, Gary Long, Farzana Khatri, Jamie Burnside, Larry Candell, and Chris Ferraiolo, who have all been of tremendous help during my time at Lincoln. Thank you also to Professors Dennis Freeman and Jeffrey Shapiro, my advisors during my time at MIT.

Thank you to my family for all their support throughout the years, Mom, Dad, Chris, Jen, and GJ. Thank you to all my friends from MIT and Milpitas who have been with me through the good times and the bad, and especially thank you to Mark.

Contents

List of Figures

List of Tables

Chapter 1

Introduction

1.1 The Mars Laser Communication Demonstration (MLCD)

The desire to gather more sophisticated science data, such as multi-spectral imagery, SAR imagery, and HDTV, during future space exploration missions to the outer planets calls for increased communication data rate capabilities of 10-100 Mbps and higher. Currently, we use the Deep Space Network, a network of antennas in California, Spain, and Australia, on the Earth receiving end. With such a system, we can support between 100 kbps - 1 Mbps Radio Frequency (RF) data rates from Mars, a factor of at least 100 less than our desired capability [8]. Table 1.1 shows the data rates required for various science data products [5].

A study carried out at Caltech's Jet Propulsion Laboratory (JPL) on current and

Space Science Data	**Data Rate**
Planetary Images	10-100 kbps
Multi-Spectral Imagery	100 kbps - 1 Gbps
Synthetic Aperture Radar	100 kbps - 100 Mbps
Video (MPEG-1 to Raw Studio Quality)	1-100 Mbps
HDTV	10 Mbps - 1 Gbps

Table 1.1: Data rates required for various science data products

expected future laser communication technology capabilities suggests that an optical communication system can achieve the data rates desired for deep space communications [6, 2]. As part of the ongoing effort to develop the capability of high data rate deep space communications, MIT Lincoln Laboratory, JPL, and NASA are working on the Mars Laser Communication Demonstration (MLCD) project. For this project, a laser communication system will be added to one of NASA's currently funded programs to launch a communication satellite, the Mars Telesat Orbiter (MTO), to Mars in 2009. During the course of the MTO mission, the MLCD project will demonstrate the capability of achieving 1-30 Mbps data rates from Mars using 1.06-μm-wavelength laser communications.

The gain in achievable data rates for optical communications systems over RF systems comes from a number of parameter values, including the transmitted signal power, the beam divergence given by the communication wavelength and transmitter diameter, the receiver area, and noise. The gain of the optical over the RF system data rates follows the theoretical dependency:

$$\frac{\text{Optical data rate}}{\text{RF data rate}} = \frac{P_{opt}}{P_{RF}} \cdot \frac{\left(\frac{\lambda_{RF}}{D_{RF}}\right)^2}{\left(\frac{\lambda_{opt}}{D_{opt}}\right)^2} \cdot \frac{R_{opt}^2}{R_{RF}^2} \cdot \frac{N_{RF}}{N_{opt}} \tag{1.1}$$

where P is the transmitted power, λ is the communication wavelength, D is the transmitter diameter, R is the diameter of the receiver telescope, and N is the noise term. For systems configured as in Table 1.2, where the noise term in the RF case is at the thermal limit and the noise term in the Optical case is higher than the thermal limit, the optical system would be capable of achieving data rates 30 times those of the RF system.

One of the key advantages of using a laser communication system over an RF system comes from the difference in beam divergence for each system, determined by λ/D. A Ka-band beam through a 2 m diameter aperture in an RF system would spread out over fractions of a degree, whereas for a laser communication system a 1 μm beam through a 30 cm aperture only spreads on the order of microradians [9]. For a communication system from Mars, an RF beam could spread to several times

Parameter	Optical	Ka-band RF
Transmitted Power	5 W	100 W
Wavelength, λ	1.06 μm	1 cm
Transmitter Diameter	30.5 cm	2 m
Receiver Diameter	5 m	60 m
Noise	600 kT/bit	2 kT/bit
Expected max data rate	30 Mbps	1 Mbps

Table 1.2: Optical and RF system parameters

the diameter of the Earth, whereas a laser beam would only cover a small portion of the Earth's surface. The narrow laser beam thus focuses an increased fraction of the total signal power on the Earth receiving station, leading to lower required transmitted signal power and thus a lower-power spacecraft system overall that is more conducive to deep space missions. The tradeoff with laser communications comes from the increased precision required to point such a narrowly focused beam.

For the MLCD mission, the laser beam will need to be pointed at the ground station with a precision of within 10% of the laser beamwidth, whereas the orbital dynamics of the satellite, Mars, and Earth, jitter in the spacecraft, and noise in the optical system itself, will cause disturbances that are hundreds of times larger and over a wide range of frequencies. To aid in the pointing and tracking, an uplink beacon signal could be pointed from the ground station to the spacecraft to provide a reference to the spacecraft of where to point the transmitted downlink beam. Unfortunately, the power required to generate a beacon signal suitable for tracking fast enough to maintain the high data rate downlink is prohibitive, on the order of kilowatts. For the MLCD mission, a new scheme for pointing and tracking must be developed to meet this challenge.

1.2 Flight Terminal Pointing and Tracking Architecture

A variety of systems will be used to stabilize the laser beam for the downlink between the Mars satellite and the Earth ground receiving station. A near-infrared imaging system consisting of a filter, telescope, and focal plane array camera will be carried on board the spacecraft in support of a beacon-tracking system for stabilization due to disturbances from DC to 0.02 Hz, and an Earth-tracking system for stabilization due to disturbances from 0.02 to 2 Hz. In addition to mechanical isolation schemes, a Magneto-hydrodynamic Inertial Reference Unit (MIRU) will be used to stabilize the laser beam against frequency disturbances of 2 Hz and higher. For the purposes of the MLCD communication downlink, the combined systems need to achieve 0.35 μrad pointing accuracy. Analogously, the MLCD mission is trying to achieve the accuracy required to point a laser beam at a dime that is 30 km away.

During initial acquisition of the beacon and thus the location of the receiver on the Earth's surface, the pointing and tracking system will first be stabilized against disturbances at higher frequencies using the mechanical isolation systems and the MIRU. Then, there will be an Earth acquisition phase in which the Earth is located in the focal plane array image. Once the Earth has been found, beacon acquisition and synchronization operations are performed. During subsequent pointing and tracking, the beacon will always be the absolute pointing reference of where to find the receiver, but, due to long integration times to build up sufficient signal-to-noise ratio, the beacon cannot be tracked alone at a sufficiently high enough rate to maintain the downlink. Thus, between beacon location measurements, the Earth will be tracked to provide the expected relative position of the beacon in each frame compared to the last known absolute location.

1.3 Thesis Goals and Approach

This thesis focuses on the design of an Earth-tracking system for the MLCD mission that will stabilize the laser beam from jitter in the frequency range of 0.02 to 2 Hz. By tracking the movements of the Earth in the onboard camera images over time, we will be able to determine what corresponding changes are needed in the pointing direction of the laser beam. For the Earth-tracking system, the 0.35 μrad pointing accuracy requirement translates to 0.089-pixel rms, 2-axis accuracy if the pixel resolution of the camera matches the diffraction limit of the telescope. Four possible Earth-tracking algorithms were implemented and their expected tracking performance evaluated under the conditions of the MLCD mission. The algorithms tested, in order of increasing complexity, were a plain centroid tracking algorithm, a centroid tracking algorithm based on thresholded Earth pixels, an FFT-based cross-spectrum phase correlation method, and an optical flow algorithm.

Before any of the candidate tracking algorithms could be tested, a data set of Earth image sequences that would be seen during the MLCD mission had to be assembled. Unfortunately, there was no extensive set of 1-μm Earth image data from Mars available to use for testing of the Earth-tracking system. As a result, a need arose to generate simulated Earth image sequences to test the performance of any Earth-tracking systems. A rough simulation of single-point-in-time images of the Earth, made previously by another member of the MLCD team, used information about the orbital dynamics of the mission to create constant-surface-albedo Earth disks of the correct size and shape (or phase angle) for any day of the mission, and with appropriate signal flux. As part of this thesis, this simulation was improved to incorporate more parameters of the MLCD mission to create a more accurate simulation of Earth image sequences. In particular, a surrogate Earth image data set was found to add surface albedo variations to the Earth disks, and the overall simulation was adapted to incorporate specifications for the optical fluctuations, noise, and spacecraft jitter during the mission. In doing so, the simulation was able to create Earth image sequences that would more closely resemble what the Mars satellite

camera might see over time.

After suitable test data had been created, the algorithms were implemented in MATLAB and their performance under MLCD mission conditions tested. Since the final sensor configuration of the camera had yet to be determined when this research was begun, the algorithms were tested under a variety of possible sensor resolutions across a range of Earth phases. Due to limited computational resources on the satellite, there was a constraint on the complexity of the algorithms in terms of processing power at the camera frame rate, thus limiting the types of algorithms that could be considered and affecting the overall choice of algorithm for the Earth-tracking system. Algorithms with acceptable performance levels were implemented in C++ on the Motorola PowerPC microprocessor that will be used on the satellite, and the computational costs evaluated by another member of the project team.

Once the algorithms had been sufficiently evaluated for Earth tracking, a recommendation was made to the project team as to which algorithm should be used on the MLCD mission. A centroid-tracking algorithm based on tracking the centroid of all pixels passing a data-driven threshold of Earth pixels was chosen for its accuracy, simplicity, and low computational cost.

The use of an algorithm that relied on an optical centroid or center of brightness raised certain issues about the use of the Earth as a tracking reference. The Earth's albedo varies across the Earth's surface at the imaging wavelength of 1.06 μm, and this variation is not constant in time. During the testing and evaluation of all the algorithms, the Earth's surface in successive camera frames was kept constant over the short periods of time between measurements of the Earth's absolute location from the beacon-tracking system, as it was assumed that the albedo variations in time would not be significant enough to affect the tracked Earth locations returned by each algorithm. In addition, the spatial albedo variations across the Earth's surface raised questions about the relative locations of the center of brightness of the Earth image and the physical center of the Earth. Knowing the relationship between these two locations is important in the signal acquisition operations of the mission. Once the Earth's location has been determined, the beacon must be located on the Earth's

surface. Information will be stored in memory on how to find the beacon using simple geometric calculations from the location of the Earth's physical center. Thus, knowing the difference between the optical and physical center of the Earth provides a search area in which to look for the beacon signal. To address these issues regarding the variability of the Earth's surface albedo in space and time, the effects of spatial and time albedo variations on the Earth's centroid and the implications for a tracking system were analyzed to prove that the Earth can in fact be used reliably as a tracking reference.

1.4 Thesis Outline

Chapter 2 discusses the development of a simulated Earth image sequence data set to use in the algorithm testing process. It describes the phenomenology of the Earth-tracking system and the parameters used to determine an accurate system model. The use of a surrogate data set of Earth images taken from the moon and adapted to fit the parameters of the MLCD mission is presented.

Chapter 3 describes the candidate tracking algorithms implemented in software and tested for the Earth-tracking system in MATLAB. Their performance under various sensor configurations and under different mission conditions is evaluated, and an algorithm is chosen for the MLCD mission based on performance and computational costs.

Chapter 4 discusses some of the issues raised from using the chosen algorithm, centroiding on a thresholded Earth. In particular, this section analyzes the effects of the Earth's albedo on a tracking system based on a centroiding algorithm, and the reliability of the Earth as a tracking reference for such a system is discussed. The results of centroiding experiments performed in the lab with the actual camera that will be used in the MLCD mission are also presented.

Chapter 5 summarizes the efforts of this thesis.

Chapter 2

Generating Simulated Earth-Image Sequences

A test data set of Earth image sequences is required in order to evaluate the performance of the candidate Earth-tracking algorithms. The desired set would be images taken of the Earth from Mars using a 1-μm imaging wavelength, preferably over a wide range of Earth phase angles from full sunlit illumination to narrow crescents. Even if such a set were found, the images would have to be adapted to match the optical noise, orbital dynamics, and spacecraft jitter characteristics of the MLCD mission. The data set used for testing of the Earth-tracking algorithms would thus be a simulation of the kinds of images expected during the MLCD mission.

A search of image data sets from NASA missions to Mars yielded several pictures of the Earth, but none taken at 1 μm. In order to use such images, the differences between the spectral reflectance of Earth's surface constituents at 1 μm and the imaging wavelength of the images would have to be taken into account. To process the images in such a fashion could be potentially complicated. To avoid such processing, it was decided to instead find a surrogate NASA data set of Earth images taken at 1 μm, but not necessarily from Mars. This could lead to differences in the range at which the images were taken. Since these images must already undergo processing to match the orbital dynamics of the MLCD mission, any resolution differences due to the images not being taken from Mars will be accounted for and adjusted by

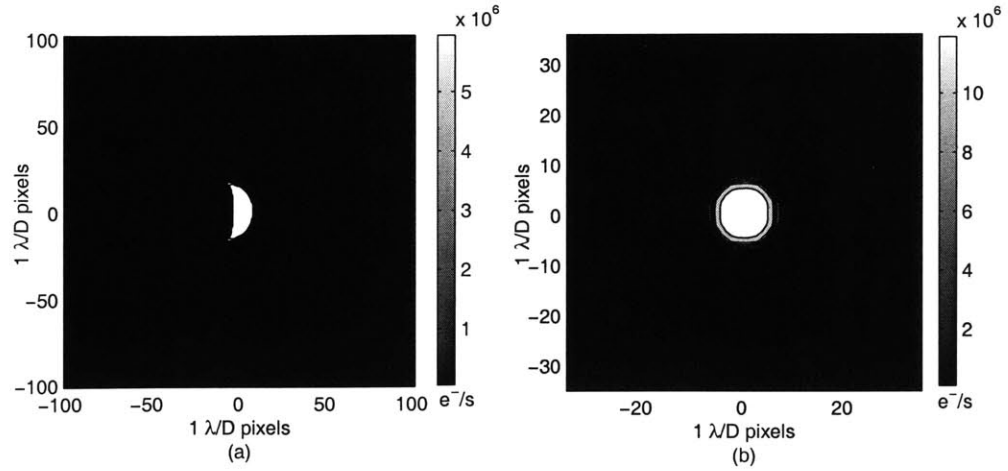

Figure 2-1: Earth images and e^-/sec generated by Farzana Khatri's simulation for the MLCD mission with 1 λ/D pixels, a) day 170 b) day 510

processing methods already being carried out, and no additional processing steps will be required. In searching for a surrogate data set, it was discovered that the 1994 Clementine mission to the moon did take several pictures of the Earth at 1 μm, and over a wide range of Earth phase angles [11]. This chapter will discuss how these images were used as a basis for generating simulated Earth image data in MATLAB on which to test the Earth-tracking algorithms.

2.1 Related Work

Farzana Khatri, a Lincoln staff member, previously created a MATLAB simulation of Earth phase and size in pixels for any given day of the Mars mission. The model produces a constant albedo surface and provides the photon flux from each Earth pixel assuming that constant surface. A sample image from Khatri's simulation is shown in Figure 2-1.

While a good starting point by taking into consideration the orbital dynamics of the mission, Khatri's simulation does not take into account the effects of the varying surface albedo or camera sensor parameters, and uses some generic optics characteristics as opposed to some more specific to the MLCD mission. The 1994 Clementine

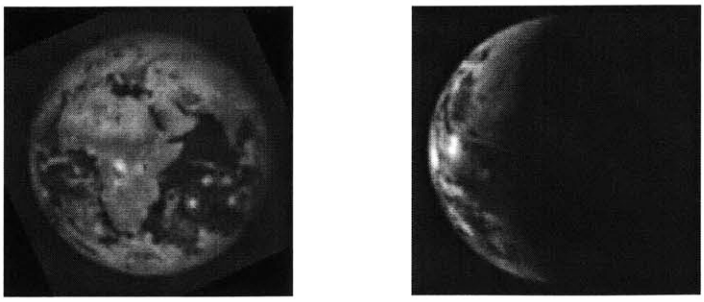

Figure 2-2: Sample Clementine mission 1-μm images of the Earth, taken from the NASA Planetary Image Atlas [11]

mission to the moon took pictures of the Earth at our desired wavelength of 1 μm $\pm$15 nm [11], a sample of which is shown in Figure 2-2.

These pictures were taken with a different camera (a Thomson TH7853-CRU-UV Si CCD), from much closer to the Earth than Mars, and with higher resolution than we will be expecting on the MLCD mission. However, these images could be used for mapping albedo variations onto the Earth shapes generated from Khatri's simulation if they are suitably rescaled to match the resolution of the MLCD Indigo ISC9809 camera. In addition, the MLCD team at Lincoln investigated the camera and sensor characteristics to determine the relevant detector parameters. This thesis discusses how these measurements were incorporated into Khatri's system model to correctly simulate the effects of the camera and detector choice on the images.

Khatri's model also only produced single-point-in-time images, and no attempt had been made to create image sequences of the Earth moving over a period of time. Jamie Burnside, another Lincoln staff member, created a simulation of the open- and closed-loop jitter expected to be seen during pointing and tracking operations of the mission. Time sequences of the corresponding movements of the camera and thus the Earth in the images were generated to match the jitter spectra of the mission, and these time sequences were used in this thesis to generate moving Earth image sequences.

2.2 Phenomenology

The rest of this chapter discusses the phenomenology of the MLCD mission and how each aspect of the system was modeled in the simulation.

2.2.1 Overview

The anticipated launch date for the MTO satellite is October 6, 2009, with almost a year of cruise time before Mars orbit insertion (MOI) on August 29, 2010. It will subsequently remain in Martian orbit for up to 2 years, for a total mission lifetime of around 1100 days. There is a desire to be able to establish a communication link on most days of the mission for a few hours each day, both during the cruise and orbit phases of the mission. As such, a wide range of pointing and tracking situations for the satellite camera will be encountered over the course of the mission. The three main parameters governing the situation seen by the camera, the satellite-to-Earth distance, the Sun-Earth-Probe (SEP) angle, and the Sun-Probe-Earth (SPE) angle, are shown in Figures 2-3, 2-4, and 2-5, respectively, for the duration of the mission. The satellite-to-Earth distance determines the size of the beacon and Earth on the camera image and the signal power received from each, the SEP angle determines the Earth phase angle seen in the image, and the SPE angle determines how close the camera is to looking at the sun when trying to point at the Earth. MLCD requirements specify a desire to be able to establish a high rate communication downlink down to a 3° SEP angle and a 2° SPE angle.

At the beginning of the mission, the higher SEP angle indicates the satellite camera will see a crescent-shaped Earth. The Earth will still be fairly close, and until approximately day 160 of the mission, the beacon on the Earth will be strong and close enough to allow for high-bandwidth (i.e., up to 2 Hz) tracking on the beacon alone. As such, only the Magneto-hydrodynamic Inertial Reference Unit (MIRU) and other high-frequency systems and the beacon-tracking system will be in operation up to day 160 of the mission, the first crossover point. One thing to note is that during

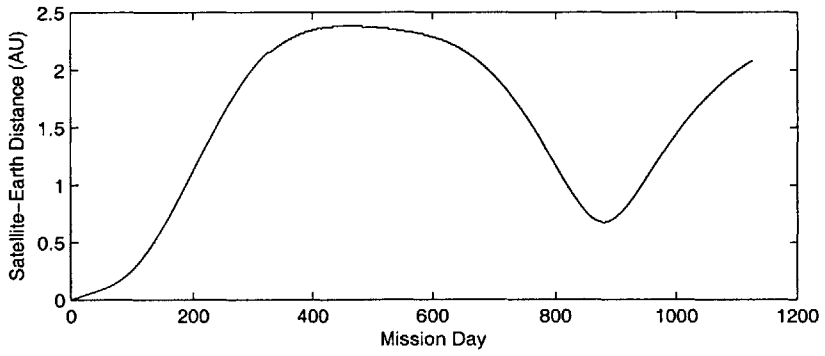

Figure 2-3: Distance between MTO satellite and Earth throughout the mission

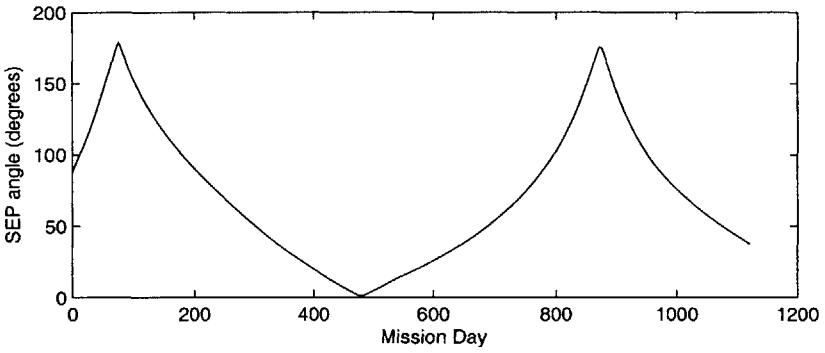

Figure 2-4: SEP angle between the Sun, Earth, and MTO satellite throughout the mission

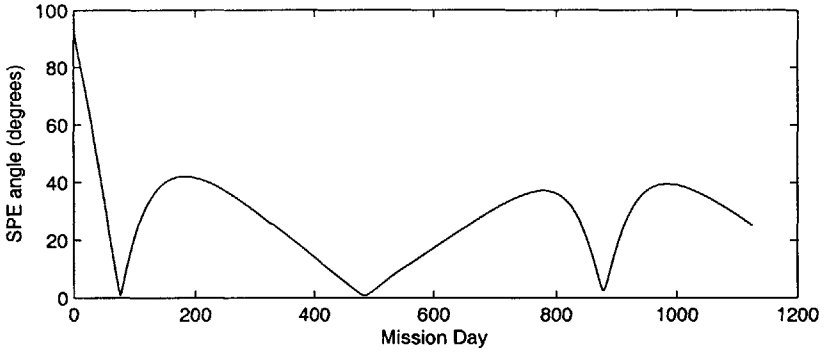

Figure 2-5: SPE angle between the Sun, MTO satellite, and Earth throughout the mission

this first part of the mission, there will be a point where the SPE angle drops below 2°. Under such conditions, the camera will be looking almost directly into the sun, and the MLCD mission will not be required to point and track or establish a downlink during this time because of the expected high photon flux and the desire not to reach full well capacity in the camera pixels.

From day 160 until the second crossover point around day 810, the beacon will be too far away and thus too weak to be used for pointing all on its own. During the bulk of the mission therefore, both the Earth-tracking and low-bandwidth (up to 0.02 Hz) beacon-tracking systems will be in operation in addition to the high frequency stabilization systems, with the Earth-tracking system responsible for frequency disturbances between 0.02 and 2 Hz. During this time, the Earth will change in phase from a crescent to a full-disk shape at day 480, and then back to a crescent again, where the Earth is simultaneously at maximum range as a full disk and at closer ranges as a crescent. Again during this phase of the mission, there will be a point when the SPE angle drops below 2°, and no pointing and tracking using the camera will occur at this time.

After day 810, there will again be a brief time when the Earth is close enough that beacon-tracking is sufficient. Finally, towards the end of the mission, the Earth-tracking system will again be needed when the third crossover point is crossed and the beacon becomes too weak for tracking on its own. Operational conditions during this period will be similar to those seen after the first crossover point at day 160.

Table 2.1 presents a summary of the different operating conditions for the lower frequency pointing and tracking systems throughout the mission.

2.2.2 From Earth to Camera Image

The processing steps for creating a simulation of Earth image sequences is presented in a conceptual block diagram in Figure 2-6. The orbital dynamics of the mission determine the size and shape of the sunlit Earth that would be seen by the spacecraft. Line-of-sight (LOS) jitter affects where the Earth lies in the field of view of the optics and camera system. As the photons of the Earth signal pass through the optics

Day	Description of Conditions
0-160	Beacon-tracking system covers up to 2 Hz
74-77	SPE angle drops below 2°, no camera tracking
160	First crossover point
160-810	Beacon- and Earth-tracking systems in use
324	Mars Orbit Insertion
480	Maximum range, full-disk Earth
480-495	SPE angle drops below 2°, no camera tracking
810	Second crossover point
810-1000	Beacon-tracking system covers up to 2 Hz
1000	Third crossover point
1000+	Beacon- and Earth-tracking systems in use

Table 2.1: Summary of camera pointing and tracking systems' operating conditions

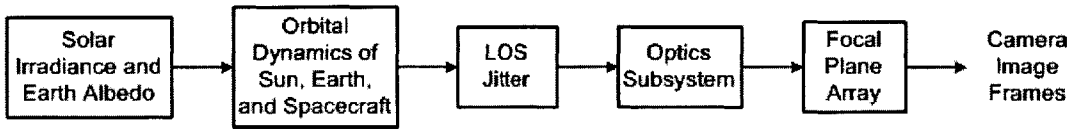

Figure 2-6: Conceptual block diagram for the Earth image simulation

subsystem, they finally land on the focal plane array of the camera. Electronic readout of the focal plane array provides the camera image frames that will be sent to the onboard processor for the Earth-tracking system.

The actual implementation in MATLAB followed a different sequence of steps that is perhaps less intuitive to the reader, a block diagram of which is presented in Figure 2-7. This chapter will follow the implementation block diagram in the discussion of the development of the Earth image simulation.

Khatri's simulation was slightly modified to provide a high resolution image of the constant albedo Earth disk. High resolution images were used because of the MATLAB processing steps required in the simulation of the optics subsystem and in the creation of image sequences from the jitter modeling step, as discussed later in this chapter. The Clementine mission images were resampled to match the resolution of these images and then mapped on to the Earth disks to add spatial albedo variations to the Earth's surface, as detailed in Section 2.2.3. The result of this step provides a

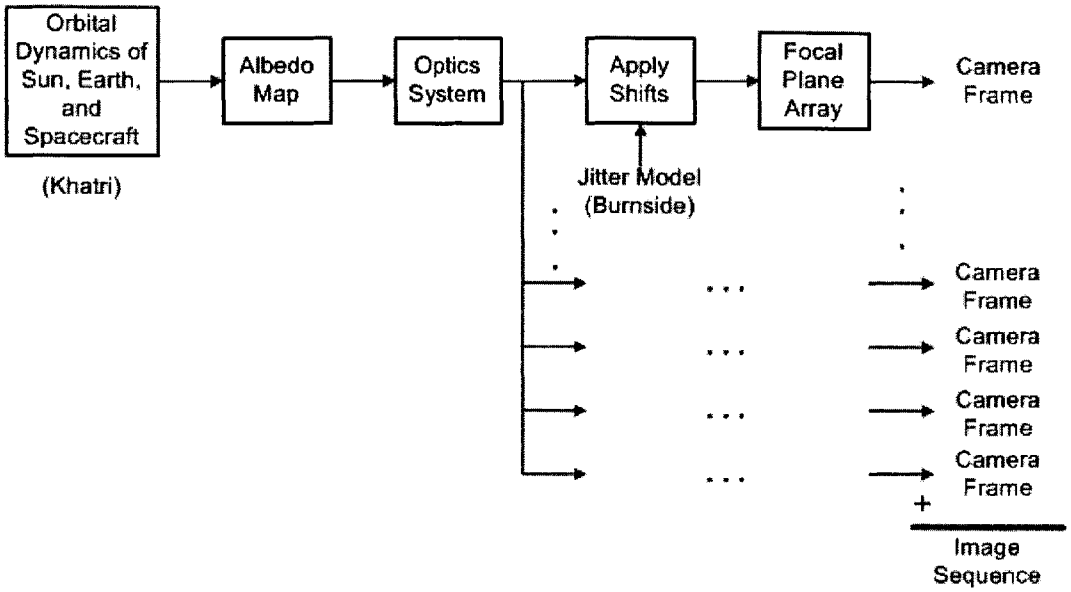

Figure 2-7: Implementation block diagram for the Earth image simulation

high resolution "image" of the expected photon flux arriving at the spacecraft.

Once the photons from the Earth arrive at the spacecraft, they pass through the optics subsystem, the modeling and simulation of which is discussed in Section 2.2.4. At this point any "shifts" in the location of the Earth due to LOS jitter are applied to the image, using information from the jitter model created by Burnside and discussed in Section 2.2.6. After passing through the various optics system components, the photons from the Earth fall on the camera's focal plane array. The modeling and simulation of the conversion from photons landing on the focal plane array's detectors to the digital numbers and the image stored in memory is presented in Section 2.2.7. During this step the image is also downsampled back to the resolution of the camera. At this point, the simulation has generated one camera frame containing an Earth image that might be expected during the MLCD mission. To create successive camera frames, the next expected shift in the image as determined by the jitter model is applied to the output of the optics subsystem step, and passed to the focal plane array modeling block to create another camera frame.

Figure 2-8 shows the simulated Earth image after each major processing block.

Earth Surface Constituents	% Reflectance at 1.06 μm
Clouds	67
Winter Snow and Ice	77
Summer Ice	46
Soil and Rocks	36
Vegetation	52
Water	7-12

Table 2.2: Percent reflectance at 1.06 μm of various Earth surfaces. Source: [14]

The major steps in the implementation of the Earth image simulation will now be discussed in the following sections.

2.2.3 Albedo Variations

The Clementine images were used to apply surface albedo variations to the Earth disks generated by Khatri's simulation of orbital dynamics. These images were taken using a 1-μm imaging wavelength and thus had correctly scaled contrasts between the different Earth surfaces to match what would be seen during the MLCD mission. The intensity of each pixel in the Clementine images corresponds to an offset plus a gain times the average albedo of the Earth's surface being imaged by that pixel. Not knowing what these offset and gain coefficients might be to recover the albedo values, it was decided instead to perform histogram range adjustment on the images to make the brightest pixel correspond to the brightest possible Earth albedo and the dimmest pixel correspond to the dimmest possible Earth albedo, with all other pixels being scaled accordingly. Albedo values, or the spectral reflectance at 1.06 μm, of various Earth surface constituents are given in Table 2.2. Manual inspection of the rescaled images verified that different surface constituents were assigned reasonable albedo values using this method.

Once the Clementine images had been converted from camera intensity to Earth albedo values on each pixel, the images had to be resized to match the MLCD mission. Bicubic interpolation was used to perform the resizing of the Clementine albedo images to have the same diameter as the corresponding high-resolution Earth disk

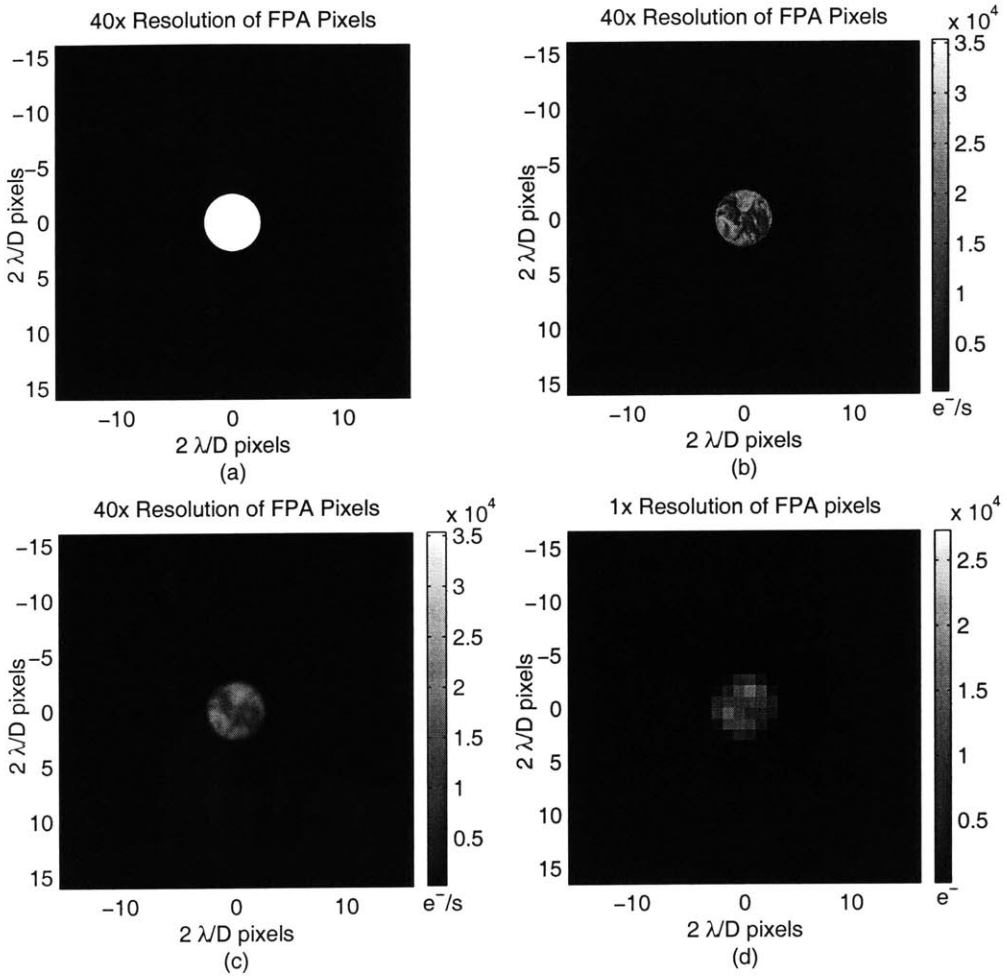

Figure 2-8: Simulated Earth image after each major processing block a) Modified Khatri Orbital Dynamics block b) Albedo Mapping (with signal flux added) c) Optics Subsystem d) Focal Plane Array

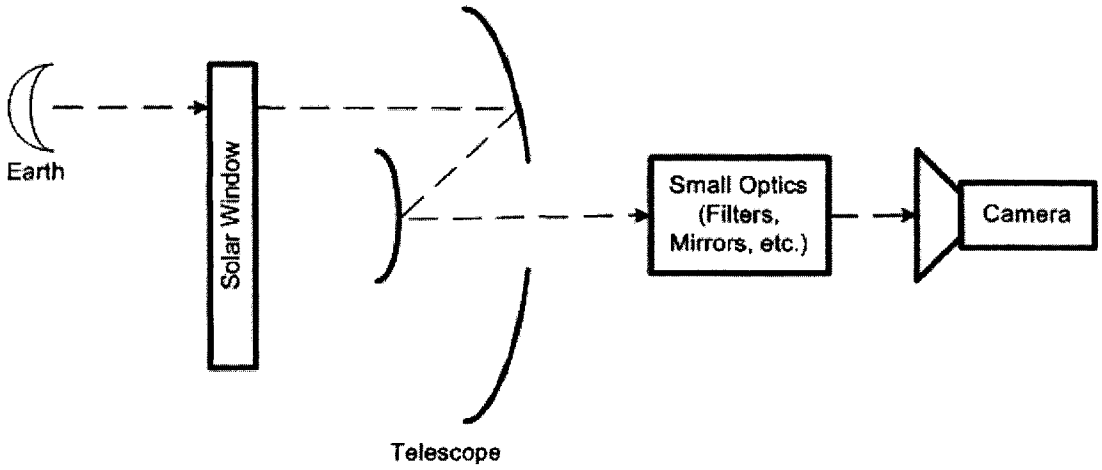

Figure 2-9: The Optics Subsystem

calculated from the modified Khatri simulation, for any day of the mission. Once the albedo image was resized to match the appropriate Earth diameter for a given day of the mission, the Earth disk shape was used to mask out all but the section of the albedo image that lined up with the sunlit fraction of the Earth. Thus surface albedo variations were added to the high-resolution Earth shapes generated by the modified Khatri orbital dynamics simulation to create a high-resolution albedo image $\rho(x, y)$.

2.2.4 Optics

A diagram of the components of the optics subsystem modeled in the simulation is shown in Figure 2-9.

Upon arriving at the optics subsystem of the spacecraft, the Earth signal first passes through the solar window filter. The filter has a 30-nm bandwidth centered around 1.06 μm to limit the amount of stray sunlight entering the optics system. Light transmitted through the solar window next passes through the telescope's 30.5 cm diameter aperture. The Earth signal will be blurred by the telescope's Airy point spread function:

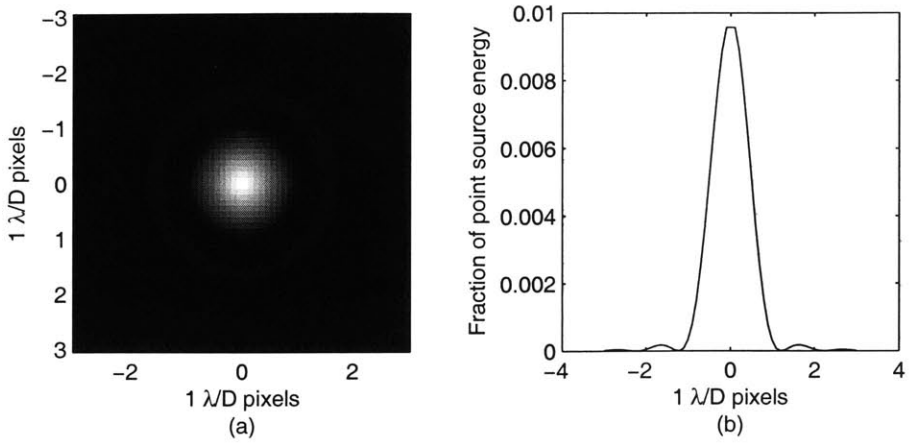

Figure 2-10: Airy point spread function for point source centered at (0,0) a) 2D point spread b) cross-section at y=0

$$Airy(x,y) = \left(\frac{2 \cdot J_1(r)}{r}\right)^2 \tag{2.1}$$

where $J_1(r)$ is a first-order Bessel function, r is given by

$$r = \left(\frac{3.83}{1.22}\right)\sqrt{x^2+y^2}$$

and (x, y) is the position on the focal plane relative to the optical axis in units of λ/D pixels. The scale factor (3.83/1.22) in r converts the location of the Bessel function zeros to their locations in units of diffraction-limited pixels. With such a point spread function, 86% of the energy from a point source would fall on one diffraction-limited pixel. Figure 2-10 shows a plot of the Airy point spread function of the telescope.

After passing through the telescope aperture, the Earth signal will pass through various small optics components, with 57.54% expected transmission of the Earth signal due to losses in the various components. Upon finally reaching the camera, the photons falling within the field of view of the camera will be detected with a quantum efficiency of 0.8.

A summary of the optics subsystem parameters modeled in the simulation is presented in Table 2.3.

Parameter	Symbol	Value	Units
Albedo	ρ	Varies	-
Energy per photon at λ=1.06μm	hc/λ	1.876e-19	J/photon
Solar Filter Bandwidth	BW	0.03	μm
Telescope Aperture Diameter	D	0.305	m
% Energy from Point Source on 1 λ/D pixel	psf	86	%
Fraction of Light Transmitted through Optics	$Loss$	0.5754	-
Quantum Efficiency	η	0.8	-

Table 2.3: Parameter values for the optics subsystem

2.2.5 Signal Level

The Earth signal comes from sunlight reflected diffusely into space and imaged onto the focal plane array. The thermal emission from the 300-K Earth is negligible at 1 μm and is not included in the calculation of the Earth signal in this simulation. The sunlight reflected from the Earth's surface in [W/m^2] at our wavelength of interest is given by

$$Reflected\ sunlight = \rho \cdot H_\lambda \cdot BW. \tag{2.2}$$

where $H_\lambda = 6.3$ W/m^2/μm is the solar irradiance on the Earth at 1 AU, centered at 1.06 μm, and ρ is the Earth albedo, which varies from 7% to 77% (see Table 2.2).

The fraction of the solid angle of Earth light received at the MTO satellite telescope aperture over the total solid angle in which Earth light radiates is given by

$$Fraction\ light\ received = \frac{\pi \left(\frac{D}{2}\right)^2}{\pi R_{ME}^2}, \tag{2.3}$$

where R_{ME} is the distance in meters between the Earth and Mars at the time the image is taken and the factor of π in the denominator comes from assuming the Earth can be modeled as a Lambertian surface.

Multiplying this fraction by the sunlight reflected from the Earth's surface gives the total Earth light in our wavelength band of interest falling on the telescope aperture in Watts per m^2 of the Earth's surface. The amount of the Earth's surface being imaged is the area of the Earth multiplied by the fraction f_E of the Earth that is

sunlit:

$$\begin{aligned} Area\ imaged &= \pi R_E^2 \cdot \frac{1}{\pi}(\sin SEP + (\pi - SEP)\cos SEP) \\ &= \pi R_E^2 \cdot f_E \end{aligned} \tag{2.4}$$

where R_E is the radius of the Earth in meters, and SEP is the Sun-Earth-Probe angle at the mission time for which an image is being simulated.

Combining equations 2.2 - 2.4 and adding in the other optics subsystem parameters, the total Earth signal flux, S_{Earth}, in [e^-/s] is given by

$$S_{Earth} = H_\lambda \cdot BW \cdot \left(\frac{\left(\frac{D}{2}\right)^2}{R_{ME}^2} \right) \cdot R_E^2 \cdot \pi f_E \cdot Loss \cdot \eta \cdot \frac{1}{hc/\lambda}. \tag{2.5}$$

This calculated S_{Earth} assumes an average albedo $\rho = 1$, as in the constant albedo Earth disk shapes generated by Khatri's simulation. Dividing the S_{Earth} signal flux evenly among all pixels in the Earth shapes gives the signal flux per pixel of albedo $\rho = 1$. Multiplying this constant albedo signal flux image by the albedo image $\rho(x, y)$ from Section 2.2.3 gives an albedo image with appropriate signal flux, designated as $S_h(x, y)$.

Adding in the effects of the Airy point spread function of the telescope, the high resolution signal flux, S_h in [photons/s] on each high resolution pixel is given by the 2-D convolution:

$$S_h(x, y) = S_0(x, y) * Airy(x, y). \tag{2.6}$$

2.2.6 Line-of-Sight Jitter

Line-of-sight (LOS) jitter in the imaging system is caused by random spacecraft motion, resonance in the vibration isolators, and the excitement of discrete bending modes in the telescope. There are two elements to the effect that LOS jitter has on the camera images of the Earth. LOS jitter at frequencies higher than the frame rate

of the camera can cause smearing in the image taken in each camera frame. LOS jitter at lower frequencies causes the apparent shifts in the Earth's location between camera frames. The jitter can be analyzed by looking at it's simulated power spectral density or as a time series of expected LOS center movements. A plot of the LOS jitter spectra from Burnside's model is shown in Figure 2-11. A time series of expected LOS movements according to the jitter model was also provided by Burnside to simulate Earth movements in the camera image simulation. Plots of sample time sequences fitting the jitter spectra are shown in Figure 2-12. Note that the LOS center shifts are given in units of diffraction-limited (1 λ/D) pixels. This was done because the tracking accuracy requirement was given in units of λ/D pixels, and it was desired to keep consistent the units of the pixel shifts applied to the Earth images and the accuracy requirement during algorithm testing.

In the simulation, the shifts in the Earth's location due to LOS jitter are applied after the optics step processing as if the shifts were only seen by the camera focal plane array, even though in the real system these shifts are seen by the entire optics system and thus "before" the convolution of the Earth light image with the Airy point spread function. This can be done because of the shift property of discrete-space Fourier transforms, yielding the same result whether the shift is applied to the Earth signal before or after passing through the telescope.

$$
\begin{aligned}
\text{If } \; S_0(x,y) * Airy(x,y) = S_h(x,y) \; &\xrightarrow{F} \; S_{0_F}(f_1,f_2)A_F(f_1,f_2) = S_{h_F}(f_1,f_2), \\
\text{then } \; S_0(x-x_0,y-y_0) * Airy(x,y) \; &\xrightarrow{F} \; e^{-j2\pi f_1 x_0} e^{-j2\pi f_2 y_0} S_{0_F}(f_1,f_2)A_F(f_1,f_2) \\
&= \; e^{-j2\pi f_1 x_0} e^{-j2\pi f_2 y_0} S_{h_F}(f_1,f_2), \\
\text{and } \; e^{-j2\pi f_1 x_0} e^{-j2\pi f_2 y_0} S_{h_F}(f_1,f_2) \; &\xrightarrow{F^{-1}} \; S_h(x-x_0,y-y_0).
\end{aligned}
$$

Therefore, $S_0(x-x_0,y-y_0) * Airy(x,y) = S_h(x-x_0,y-y_0)$.

As can be seen in Figure 2-12, the Earth-location movements expected are at the sub-diffraction-limited-pixel level, on the order of a few tenths of a diffraction-limited pixel from frame to frame and on the order of a few hundredths of 0.1-0.2

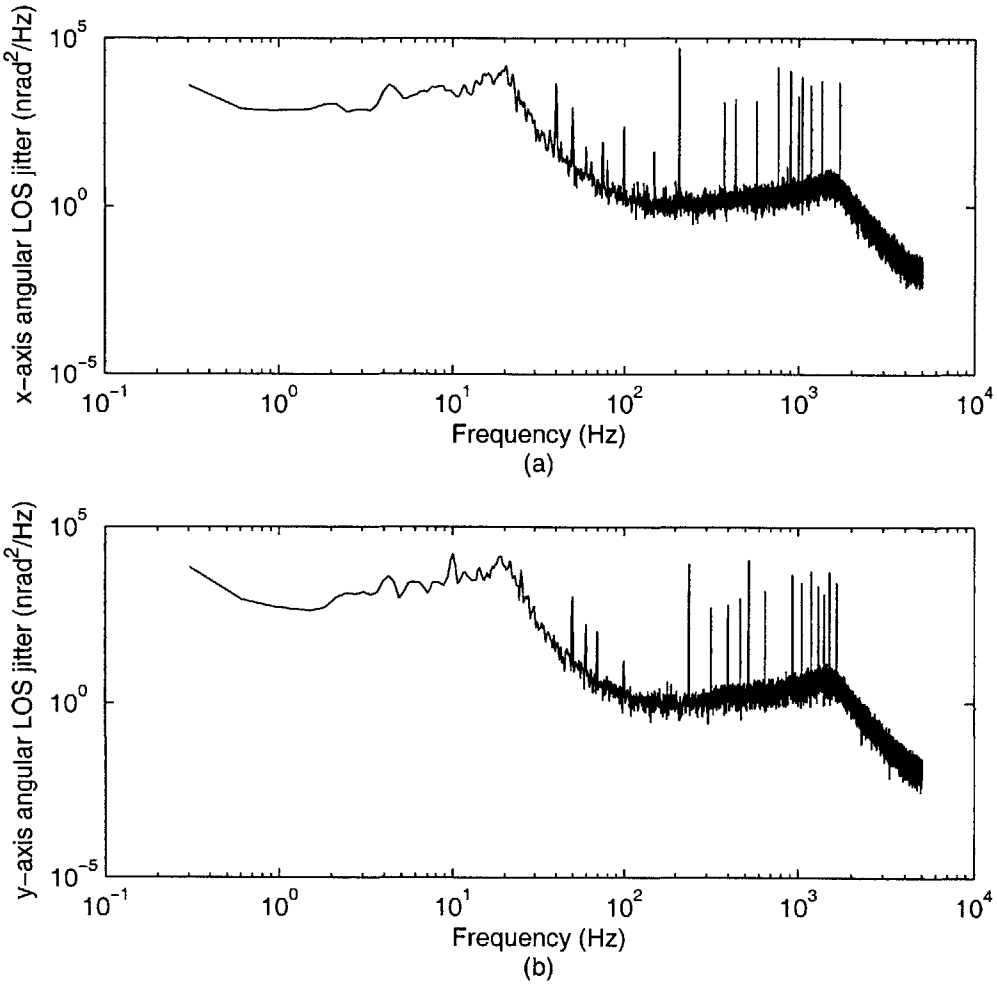

Figure 2-11: Closed-loop LOS jitter spectra provided by Jamie Burnside a) x-direction b) y-direction

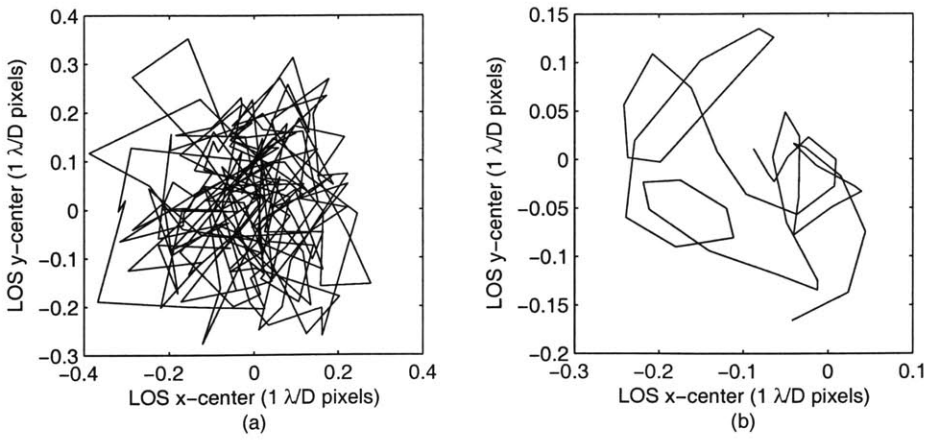

Figure 2-12: Sample LOS movements provided by Jamie Burnside in a) 1 s time period b) 4.8 ms time period. Note that the jitter is defined in units of 1 λ/D pixels

diffraction-limited pixels within each 4.8 ms timeframe. As such, the camera pixel images would also have to be shifted at the subpixel level. Thus the high-resolution images were created to allow for "subpixel" shifts (which could be rounded to integer pixel shifts in high resolution images), because subpixel-level image shifting cannot be done without interpolation. The high-resolution images were formed from the beginning in the processing steps for simulating Earth images as opposed to after the optics processing block because of the lowpass filtering of the image by the telescope's point spread function. As opposed to performing interpolation and upsampling on a blurred version of the original "picture," the interpolation was performed on the original "picture" before being passed to the optics processing block. A sample camera frame image at this point in the simulation that includes the effects of smearing is shown in Figure 2-13. As can be seen in the figure, the effects of smearing are not significant enough to be visible to the human eye.

2.2.7 Focal Plane Array

Once the light hits the focal plane array, the sensor characteristics need to be taken into account. The pixel resolution governs the pixelation of the Earth signal and will determine the number of pixels across the Earth diameter in the image. Diffraction-

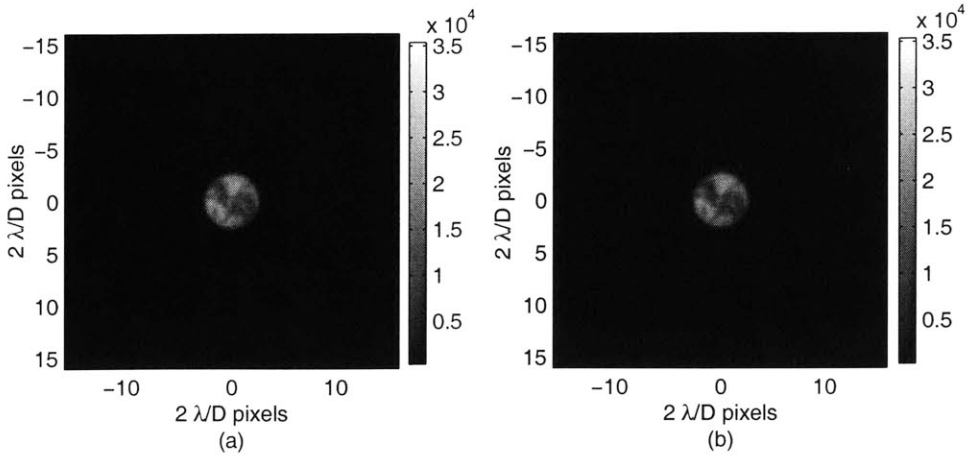

Figure 2-13: Sample camera frame image a) before smearing added b) after smearing added

limited (λ/D) pixels take advantage of the best resolution that the telescope can resolve and produces the finest detailed images. However, tradeoffs with other sensor characteristics call for a $2\frac{\lambda}{D}$ pixel resolution to provide the best images for the overall camera tracking system. The photodetectors used in the focal plane array produce a dark current, B, a bias value that is present even in the absence of light and that will be added to any signal received on each pixel. There will be an integration time, τ, associated with the camera to determine how long to integrate the photon flux from the Earth signal and the dark current in time in each frame. The signal on the detector also produces shot noise. Read noise, modeled as Gaussian with zero mean and $\sigma = n_e = 160$ e$^-$/s, or $\mathcal{N}(\mu = 0, \sigma = n_e)$, is added to every pixel each time the array is read out. For the focal plane array being used in the MLCD mission, the read noise is the dominant noise term. As such, the fewer pixels that need to be read out, the less noise there will be in the focal plane array system. Thus, $2\frac{\lambda}{D}$ pixels were chosen to cut down on the number of pixels needed to read out the Earth image and thereby lessen the noise and increase signal-to-noise ratio. For each frame, only a 32x32 pixel area containing the Earth is read out. Finally, a 14-bit A/D converter with a quantization step of $Q = 16$ e$^-$/dn converts the analog values from the array to digital numbers for processing. The simulation parameters associated with the

Parameter	Symbol	Value	Units
Pixel width	pixel	2 λ/D	radians
Dark current	B	200,000	e^-/s
Frame Rate	F_s	208	Hz
Integration Time	τ	1/208	s
Pixel Read Noise	n_e	160	e^-/frame
A/D converter #bits	b	14	bits
A/D converter quantization step	Q	16	e^-/dn

Table 2.4: Parameter values for the focal plane array

focal plane array are summarized in Table 2.4.

The high-resolution Earth image, $S_h(x, y)$, or its shifted version, is downsampled in this processing block to the resolution of the FPA by summing the signal in the area covered by each pixel to give the signal image $S(x, y)$ in [e^-/s]. The Earth image without noise in each frame is given by

$$S'(x, y) = (S(x, y) + B) \cdot \tau. \tag{2.7}$$

The signal S' is a Poisson variable so its variance is the mean. The noise term added to each pixel based on the shot and read noise is given by

$$\sigma(x, y) = \sqrt{S'(x, y) + n_e^2} \tag{2.8}$$

The number of electrons read out from each pixel is thus given by

$$Z(x, y) = \mathcal{N}\left(\mu(x, y) = S'(x, y),\ \sigma(x, y) = \sqrt{S'(x, y) + n_e^2}\right), \tag{2.9}$$

with checks made to make sure that $Z(x, y) \geq 0$ for all x and y.

The output of the focal plane array detector circuitry, $Z(x, y)$ is then passed to the A/D converter, so that the final camera frame image used for the tracking system is given by

$$I(x, y) = Z(x, y)/Q, \tag{2.10}$$

with the appropriate bound $I(x, y) \leq 2^b - 1$ for all x and y, where $2^b - 1$ is the digital readout of saturated pixels.

Sample images for various days of the mission are shown in Figure 2-14.

2.3 Limitations of the Simulation

2.3.1 Earth's Terminator

Real images showing the Earth's terminator (the day-night boundary on the Earth's surface) show a gradual transition from light to darkness, where the Earth seems to fade out as the boundary is crossed. This effect can be seen in the Clementine image shown in Figure 2-15.

These effects on the albedo image were not modeled in this simulation. The Earth shapes generated from Khatri's orbital dynamics simulation include the area where the terminator occurs, whereas the Earth albedo image is simply masked onto this shape from a full-disk image, with no additional adjustments made to handle the dimmer terminator. Although the albedo images could be processed by making adjustments based on the lighting conditions, perhaps by modeling the Earth as a non-Lambertian surface at low elevation angles, this processing was not done for this simulation. As a result, the simulated images show an abrupt transition from day to night on the Earth's surface with no fading on the terminator, as can be seen in the Day 160 image in Figure 2-14.

2.3.2 Albedo Variations in Time

While in actuality the Earth's surface albedo changes over time, due to weather and the rotation of the Earth, the albedo images were kept constant in time in the Earth-image simulation. At the resolution and frame rate at which the MTO camera will be looking at the Earth, it was assumed that the albedo variations in time would be too small and too slow to change the images from frame-to-frame enough to affect the performance of the tracking algorithms. Thus, because the simulation is only meant

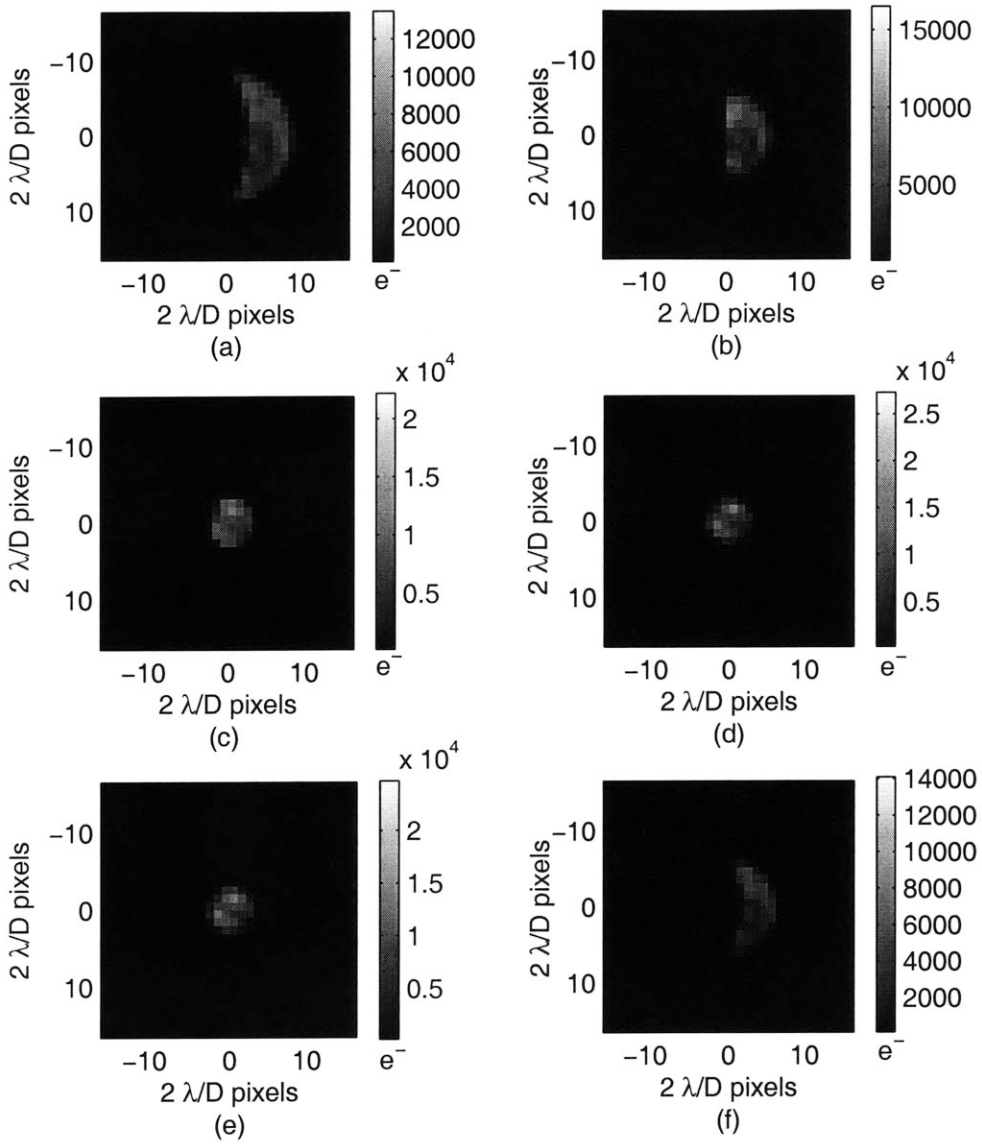

Figure 2-14: Simulated Earth images a) Day 160 b) Day 200 c) Day 300 d) Day 479 e) Day 600 f) Day 808

Figure 2-15: Clementine image showing the Earth's terminator [11]

for generating short time sequences worth of data, the Earth's time-varying albedo was not modeled in the simulation, and the validity of this assumption was verified in Section 4.2 for the chosen tracking algorithm.

2.3.3 Angular Jitter

Besides the LOS jitter that makes the Earth appear to shift/translate across the camera field of view, the spin of the spacecraft adds rotation in the images. However, the rotation rate is too slow to be seen noticeably in the images at the frame rate being used by the camera, and its effects were not included in the simulation.

2.3.4 FPA Pixel Gain and Offset Non-Uniformity

One aspect of the focal plane array characteristics not included in the simulation was the non-uniform gain and offset associated with each photodetector in the conversion from photons to electrons. This non-uniformity will be compensated for through calibration during the mission to have a residual non-uniformity less than 0.02%. The effects of the residual non-uniformity on the tracking system were assumed to be insignificant and thus were not included in the simulation. For the purposes of the simulation, a uniform offset of 0 and gain of 1 were assumed across the FPA.

Chapter 3

Tracking Algorithms

Once simulated Earth image sequences were generated and the phenomenology of the system known, algorithms could be selected for the Earth-tracking system. As discussed in Section 2.2.6, the movements in the Earth's location from one frame to the next are expected to be at the subpixel level. Rotation and scaling will be insignificant in the frequency range and at the distances for which the Earth-tracking system is in operation. Between measurements of the Earth's absolute location from the beacon-tracking system, Earth albedo variations in time (due to weather patterns and the Earth's rotation about its axis), are also expected to be insignificant, and thus the albedo image mapped onto the Earth disk can be kept constant over successive camera frames. Determining the shift in the Earth's location between camera frames thus becomes similar to an image registration problem where the expected transformation from one image to the next is a pure, subpixel translation. The pointing requirements on the laser beam call for the Earth-tracking system to have a 0.089-diffraction-limited-pixel rms, 2-axis accuracy. The algorithm must also run within the 4.8 ms frame time along with other algorithms and processes that must be run each frame as well. This constraint on computational complexity is secondary to the accuracy requirement and could have been relaxed if no algorithms were found to meet both the accuracy and computational cost requirements. Fortunately, an algorithm was found that met both requirements. This chapter discusses the candidate subpixel image registration algorithms for the Earth-tracking system and the test results that

led to the selection of the segmented-Earth centroid tracking algorithm using image thresholding for the MLCD mission.

3.1 Related Work

An immense amount of research has been done on image registration problems, including algorithms for subpixel motion and thus subpixel accuracy applications. Three classes of algorithms were chosen for evaluation as candidates for the MLCD mission. Centroid tracking is widely used in space applications. It is simple and very computationally efficient, and often provides sufficient accuracy for tracking applications. A variation of the centroid algorithm using image thresholding [12] to segment out only the Earth pixels for centroiding was also tested in this thesis. An FFT-based cross-spectrum phase correlation method [1, 13] that approaches the registration problem from the frequency domain was also selected because of it's capability of registering a wider variety of scenes and it's efficient computation through the use of FFT's. Finally, a differential optical flow algorithm [7] was tested despite it's computational cost because of it's high registration accuracy should the other algorithms fail to meet the accuracy requirement.

MATLAB functions implementing the FFT-based cross-spectrum phase correlation method and the optical flow algorithm were previously developed by Gary Long at Lincoln. His code was used for this thesis to test these two algorithms.

3.2 Description of the Algorithms

This section will describe the algorithms that were tested to determine their performance in estimating the shift (x_0, y_0) between two images x_1 and x_2:

$$\mathrm{x}_2(x, y) = \mathrm{x}_1(x - x_0, y - y_0) \tag{3.1}$$

3.2.1 Centroid Tracking

The centroiding algorithm finds the location of the optical center of brightness in each image, using only Earth pixels in the centroiding calculation for the thresholded-centroiding algorithm and using all pixels in the image for the plain centroiding algorithm. The centroid calculation of a $2N \times 2N$ pixel array is given by

$$C_x = \frac{1}{S}\left\{\sum_{i=1}^{N}(i-\frac{1}{2})\left[\sum_{j=-N}^{N} S_{ij} - \sum_{j=-N}^{N} S_{-ij}\right]\right\} \tag{3.2}$$

and

$$C_y = \frac{1}{S}\left\{\sum_{j=1}^{N}(j-\frac{1}{2})\left[\sum_{i=-N}^{N} S_{ij} - \sum_{i=-N}^{N} S_{-ij}\right]\right\} \tag{3.3}$$

where S_{ij} is the signal intensity on the (i,j) pixel, S is the total signal in the image summed over all pixels, and the pixels are labeled $[-N,...-1,1,...N]$ with no "0" pixel (the point (0,0) lies at the intersection of the four center pixels in the image). The shift between the two images was found by finding the difference between the locations of the Earth's centroid in the two images.

Segmentation of the Earth pixels was implemented as an essential preprocessing step after a background pixel bias was discovered in the centroid calculation when all of the background pixels were included. If the origin is placed at the optical axis at the center of the image, then the many space background pixels tend to dominate the few Earth pixels and bias the centroid towards the center of the image. The further the Earth is located radially away from the center of the field of view and the origin of the centroid calculation, the more effect this background bias will have in generating an incorrect Earth centroid location, as illustrated in Figure 3-1.

To segment the Earth pixels, simple thresholding was sufficient to separate the bright Earth from the space background. The proposed threshold for testing was based on the mean background signal plus six times the standard deviation of its read and shot noise, $B\tau + 6\sigma_b$, where $\sigma_b = \sqrt{B\tau + n_e^2}$. During the mission this threshold can be calibrated through measurements of the background mean and rms values

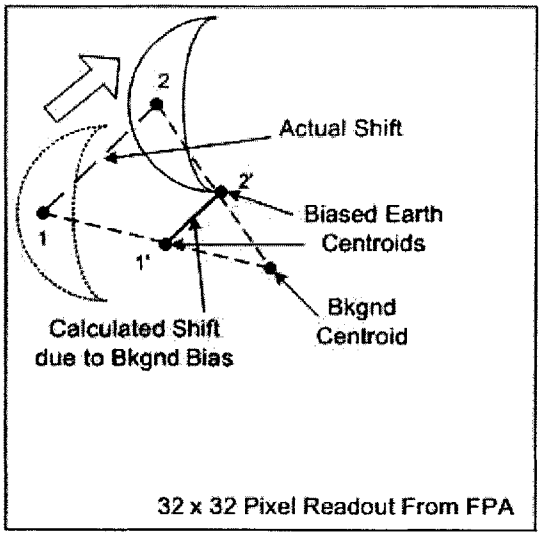

Figure 3-1: Illustration of the effects of the background in shifting the Earth centroid location towards the center of the image, resulting in incorrect shift estimations by a plain centroiding algorithm due to this background bias

before each communication pass. No other similarly bright objects come into the 0.11° field-of-view of the 32x32 pixel grid read out for the Earth-tracking algorithms to warrant a more complex segmentation algorithm. As discussed previously, no laser communications will take place when the spacecraft is pointing at an SPE angle within 2° of the sun. The closest pass of other planets comes from a 0.31° separation between the Earth and Mercury, again too large a separation for both the Earth and Mercury to be in the field-of-view at the same time. Finally, examination of star catalogs revealed that only 16 stars are above the noise level in the field-of-view throughout the mission, but all are still too dim to be above the proposed threshold.

3.2.2 FFT-Based Cross-Spectrum Phase Correlation

The FFT-based cross-spectrum phase correlation method tackles the problem by transforming to the frequency domain, and is described more fully in Averbuch *et al.* [1] and Stone *et al.* [13]. A shift in space in an image becomes a phase shift in the frequency domain. For two successive camera frames with a shift x_0 in the x-direction

and y_0 in the y-direction between them, we then have

$$\mathrm{x}_1(x,y) \xrightarrow{F} \mathrm{X}_1(f_1,f_2) \tag{3.4}$$

$$\mathrm{x}_2(x,y) \xrightarrow{F} \mathrm{X}_2(f_1,f_2) = e^{-j2\pi f_1 x_0} e^{-j2\pi f_2 y_0} \mathrm{X}_1(f_1,f_2). \tag{3.5}$$

This phase shift can be isolated by calculating the normalized cross spectrum

$$\begin{aligned} \frac{\mathrm{X}_1^*(f_1,f_2)\mathrm{X}_2(f_1,f_2)}{|\mathrm{X}_1(f_1,f_2)||\mathrm{X}_2(f_1,f_2)|} &= \frac{|\mathrm{X}_1| e^{-j2\pi f_1 x} e^{-j2\pi f_2 y} |\mathrm{X}_1| e^{j2\pi f_1 x} e^{j2\pi f_2 y} e^{-j2\pi f_1 x_0} e^{-j2\pi f_2 y_0}}{|\mathrm{X}_1||\mathrm{X}_2|} \\ \frac{\mathrm{X}_1^*(f_1,f_2)\mathrm{X}_2(f_1,f_2)}{|\mathrm{X}_1(f_1,f_2)||\mathrm{X}_2(f_1,f_2)|} &= e^{-j2\pi f_1 x_0} e^{-j2\pi f_2 y_0}. \end{aligned} \tag{3.6}$$

Averbuch *et al.* [1] uses the normalized cross spectrum and its inverse Fourier transform, the phase correlation function $PC(x,y)$, to iteratively find the shift between the two images with subpixel accuracy. Stone *et al.* [13] adds improvements to the method when aliasing is present in the images by detecting and removing Fourier components that have been affected by aliasing and are thus unreliable to use in calculating the shift between the two images.

3.2.3 Optical Flow

The optic flow algorithm uses the constant brightness assumption to estimate the velocity of the scene as it moves through the camera field of view in the two images [7]. The constant brightness assumption specifies that

$$uE_x(x,y,t) + vE_y(x,y,t) + E_t(x,y,t) = 0 \tag{3.7}$$

where E_x, E_y, and E_t are the gradients of the brightness image of the scene $E(x,y,t)$ with respect to x, y, and t, respectively, and u and v are the velocities of the scene in the x- and y-direction, respectively.

Equation 3.7 is given for every pixel, and we are looking for the u and v that holds for all pixels between the two images. Because the images are noisy and we are only able to calculate discrete estimates of the gradients E_x, E_y, and E_t at each pixel,

we can only calculate the best-fit u and v to minimize the error from the constant brightness assumption:

$$\varepsilon = \sum_{x,y} (E_x u + E_y v + E_t)^2 \tag{3.8}$$

Minimizing the error ε yields the minimum-mean-squared-error (MMSE) estimates of the scene velocity, $(\hat{u}, \hat{v})$, given by

$$\begin{bmatrix} \hat{u} \\ \hat{v} \end{bmatrix} = \begin{bmatrix} \sum E_x^2 & \sum E_y E_x \\ \sum E_x E_y & \sum E_y^2 \end{bmatrix}^{-1} \begin{bmatrix} \sum E_x E_t \\ \sum E_y E_t \end{bmatrix}. \tag{3.9}$$

Once the scene velocity is known, multiplying by the time between images gives the estimated shift (x_0, y_0) between the two images.

A coarse-to-fine approach [3] was also used in the implemented optic flow algorithm to smooth the image and remove noise, to obtain a first guess of the shift between the two images at lower resolution, and then repeat using the knowledge from this first guess to get increasingly precise estimates of the shift with higher resolution images.

3.3 Algorithm Performance

3.3.1 Testing Method: The 1 λ/D Case

To test the algorithms, the simulation described in the previous chapter was used to create test data sets where each image had been shifted by some known subpixel amount from a reference image. Because the pointing-accuracy requirement and jitter time series were given in units of diffraction-limited (i.e. 1 λ/D) pixels, the test shifts applied to the reference image were also in sub-1-λ/D-pixel amounts. Specifically, each data set consisted of 441 images where a base image was shifted by $(x_0, y_0) = (0.05n, 0.05n)$ λ/D pixels for $n = 0, 1, ...20$, giving 440 shifts (x_0, y_0) ranging from (0,0) to (1,1) λ/D pixels in a 1x1 diffraction-limited-pixel square area. These shifts were applied at high resolution (as discussed in Section 2.2.6) and all images were then "pixelated," or downsampled, and noise was added to each image to create the

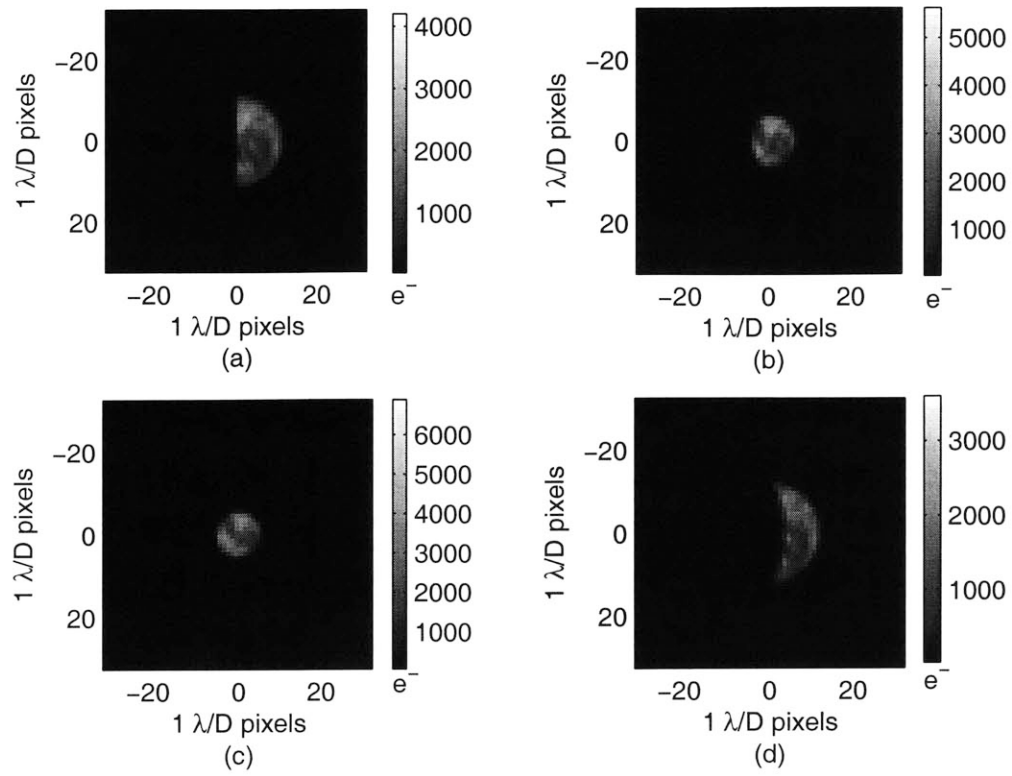

Figure 3-2: Base images at 1 λ/D pixel resolution a) Day 200 b) Day 300 c) Day 479 d) Day 808

simulated MLCD camera images. The initial MLCD camera design had specified the use of diffraction-limited pixels, and was not changed to 2 λ/D pixels until months after this research was begun. As a result, test data was generated and tests were initially run assuming that diffraction-limited pixels would be used.

The algorithms were tested on images representing a range of Earth phase angles that would be seen throughout the mission, in case the shape of the object being tracked affected the performance of the algorithms. The base images used were thus sample images from: Day 200, where the Earth is a half disk; Day 300, where the Earth is three-quarters full; Day 479, where the Earth is a full-disk and at maximum range; and Day 808, where the Earth is a small crescent. Pictures of the base images at 1 λ/D pixel resolution are included in Figure 3-2.

For example, the sample image from day 479 of the mission would be shifted

Algorithm	Day	Max Error	Avg Error	% $\leq$ 0.089
Plain Centroiding	200	1.1768	0.5966	0.68
	300	1.2049	0.6470	1.14
	479	1.1852	0.6433	0.22
	808	1.3251	0.6910	0.22
Thresholded-Centroiding	200	0.0502	0.0194	100
	300	0.0248	0.0104	100
	479	0.0271	0.0104	100
	808	0.0744	0.0210	100
CS Phase Correlation	200	0.0581	0.0213	100
	300	0.0450	0.0186	100
	479	0.0516	0.0237	100
	808	0.0768	0.0315	100
Optic Flow	200	0.0528	0.0205	100
	300	0.0443	0.0225	100
	479	0.0396	0.0196	100
	808	0.0662	0.0259	100

Table 3.1: 1 λ/D pixel resolution algorithm error statistics for varying Earth phase: maximum radial 1-λ/D-pixel error, average radial 1-λ/D-pixel error, and % errors meeting the 0.089-radial-diffraction-limited-pixel accuracy requirement

by multiples of 0.05 diffraction-limited pixels at high resolution in the x- and y-direction to create 440 shifted images with the original image as the base image, all downsampled to a 1 λ/D pixel resolution, to create a set of 440 base-image/shifted-image pairs. Each image pair in the set was supplied to a tracking algorithm that tried to estimate the shift between the images, and the radial error between the estimated and actual shifts was recorded. The 440 calculated radial errors were then accumulated to compute error statistics on the maximum radial 1-λ/D-pixel error, average radial 1-λ/D-pixel error, and percentage of the errors meeting the 0.089 radial diffraction-limited-pixel accuracy requirement for that algorithm and test set, and compared to the error statistics of the other algorithms for the same test set. Table 3.1 includes these error statistics for all of the tested algorithms when using 1 λ/D pixels.

As can be seen in the table of error statistics, adding a thresholding processing step to the centroiding algorithm yields big improvements in performance over a plain

centroiding algorithm. The thresholded-centroiding algorithm, cross-spectrum phase correlation method, and optic flow algorithm all performed well at the original 1 λ/D pixel resolution, across the range of Earth phase angles tested. The maximum and average errors were higher for the crescent shapes, but each of these three algorithms still met the accuracy requirements for all shifted images tested.

The thresholded-centroiding algorithm and the cross-spectrum phase correlation method were implemented in C++ on the MLCD mission's Motorola PowerPC microprocessor by Lincoln's David Baron to evaluate their computational costs. Optic flow was not implemented in C++ because it was assumed it's computational costs would be greater than the other algorithms. Execution time for the thresholded-centroiding algorithm was on the order of 300 μsec, while for the cross-spectrum phase correlation method the execution time was on the order of a few milliseconds. Unfortunately the cross-spectrum phase correlation method could not be reduced to a sufficiently fast execution time to run in the 4.8 ms frame time along with all of the other processes that needed to be done in that time frame. The thresholded-centroiding algorithm was thus initially chosen for the MLCD mission, although with a relaxed computational cost constraint either the cross-spectrum phase correlation method or the optical flow algorithm could have been used with 1 λ/D pixel resolution. If the mission conditions were different, specifically if the background noise was high enough that the thresholded-centroid algorithm could not properly segment out only Earth pixels for the centroid calculation, the cross-spectrum phase correlation method and optical flow algorithm should be considered.

3.3.2 Changing the MLCD Pixel Resolution: 2 and 2.5 λ/D Pixels

After the initial algorithm recommendations had been made, discussion began on the possibility of changing to the use of $\geq$2 λ/D pixels to increase the signal-to-noise ratio in support of the beacon-tracking system. While signal-to-noise would also increase for the Earth-tracking system on each pixel, the total number of pixels covered by

the Earth would decrease. Although many of the algorithms had run well using diffraction-limited pixels, there was concern over whether the decrease in number of Earth pixels on which to track would affect the performance of each algorithm.

New tests were run using test data with 2 λ/D and 2.5 λ/D pixel resolutions to see what effects varying the pixel resolution would have on the performance of the algorithms, again tested on a range of Earth phase angles. The shifts applied to each of the base images and the days tested were the same as discussed in Section 3.3.1, with the same high resolution images as before, but with the high resolution base and shifted images instead "pixelated" to the 2 or 2.5 λ/D pixel resolutions according to which resolution was being tested. The resulting base images for the 2 λ/D pixel resolution case are included in Figure 3-3 and the base images for the 2.5 λ/D pixel resolution case are included in Figure 3-4.

The same steps for testing the algorithms in the 1 λ/D case were again used for the two other pixel resolutions being tested. The 440 calculated radial errors were accumulated to compute error statistics on the maximum radial 1-λ/D-pixel error, average radial 1-λ/D-pixel error, and percentage of the errors meeting the 0.089 radial diffraction-limited-pixel accuracy requirement for each algorithm for a particular test set (defined by the test day and pixel resolution). Table 3.2 includes these error statistics for all of the tested algorithms when using 2 λ/D pixels, and Table 3.3 includes these error statistics for all of the tested algorithms when using 2.5 λ/D pixels.

At these pixel resolutions, only the thresholded-centroiding algorithm met the accuracy requirements for the MLCD mission. The maximum error seen across all test days was lower for the thresholded-centroiding algorithm when 2 λ/D pixels were used than in the 1 λ/D pixels case, though they appeared to increase again with a 2.5 λ/D pixel resolution. In particular, the change to 2 λ/D pixels appeared to improve the thresholded-centroiding algorithm's performance on crescent shapes. The increase in signal-to-noise ratio when going from 1 λ/D pixels to pixels with a larger field-of-view seems to have benefited the thresholded-centroiding algorithm for the 2 λ/D case. At 2.5 λ/D pixels however, the thresholded-centroid algorithm's performance

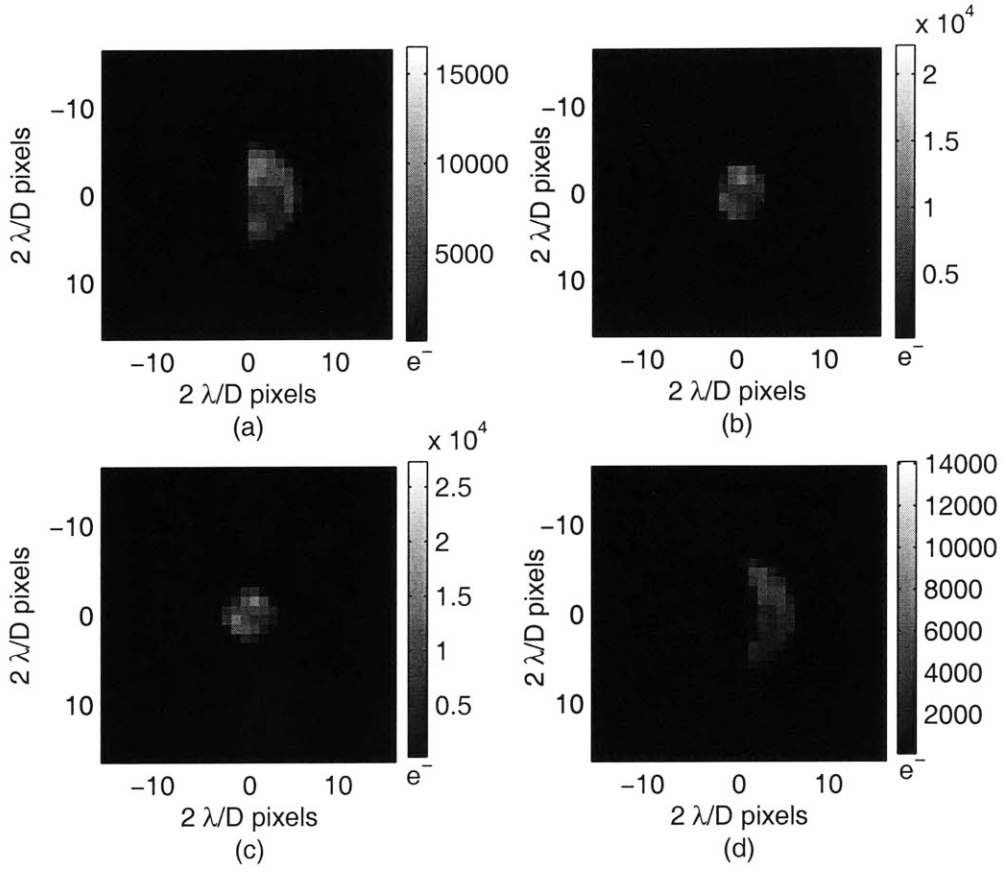

Figure 3-3: Base images at 2 λ/D pixel resolution a) Day 200 b) Day 300 c) Day 479 d) Day 808

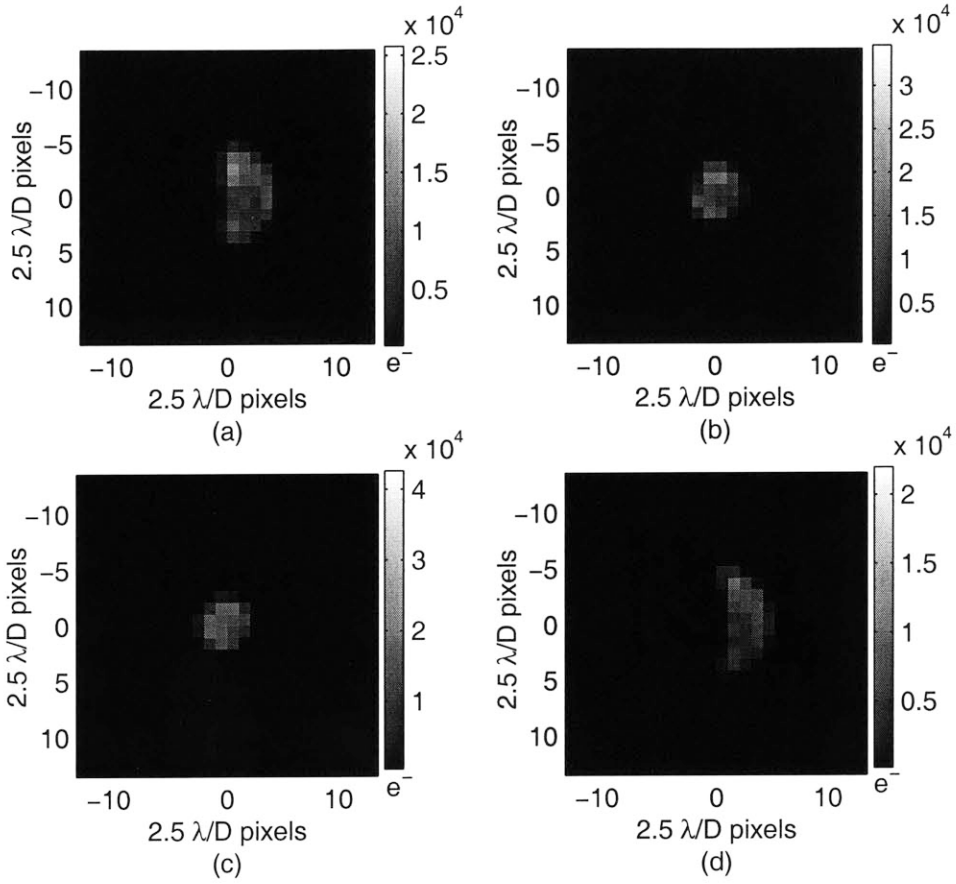

Figure 3-4: Base images at 2.5 λ/D pixel resolution a) Day 200 b) Day 300 c) Day 479 d) Day 808

Algorithm	**Day**	**Max Error**	**Avg Error**	**% $\leq$ 0.089**
Plain Centroiding	200	0.8142	0.4414	0.22
	300	0.8952	0.3626	4.09
	479	0.7588	0.2693	9.32
	808	0.8100	0.3417	3.64
Thresholded-Centroiding	200	0.0296	0.0119	100
	300	0.0259	0.0073	100
	479	0.0303	0.0151	100
	808	0.0559	0.0249	100
CS Phase Correlation	200	0.0759	0.0412	100
	300	0.0570	0.0249	100
	479	0.1079	0.0707	76.59
	808	0.1623	0.1000	36.82
Optic Flow	200	0.1330	0.0245	97.50
	300	0.1021	0.0587	94.32
	479	0.1339	0.0536	84.55
	808	0.1250	0.0747	75.00

Table 3.2: 2 λ/D pixel resolution algorithm error statistics for varying Earth phase: maximum radial 1-λ/D-pixel error, average radial 1-λ/D-pixel error, and % errors meeting the 0.089-radial-diffraction-limited-pixel accuracy requirement

Algorithm	**Day**	**Max Error**	**Avg Error**	**% $\leq$ 0.089**
Plain Centroiding	200	0.6543	0.3119	8.41
	300	0.7595	0.3754	1.14
	479	0.7446	0.3683	3.41
	808	0.8512	0.4320	2.27
Thresholded-Centroiding	200	0.0601	0.0295	100
	300	0.0391	0.0208	100
	479	0.0467	0.0223	100
	808	0.0607	0.0240	100
CS Phase Correlation	200	0.2133	0.1188	26.82
	300	0.1714	0.1012	34.55
	479	0.2066	0.1191	27.05
	808	0.2128	0.1088	11.14
Optic Flow	200	0.3221	0.1592	20.45
	300	0.2520	0.1125	38.18
	479	0.3033	0.1517	22.50
	808	0.2380	0.1179	29.55

Table 3.3: 2.5 λ/D pixel resolution algorithm error statistics for varying Earth phase: maximum radial 1-λ/D-pixel error, average radial 1-λ/D-pixel error, and % errors meeting the 0.089-radial-diffraction-limited-pixel accuracy requirement

appeared to decrease again, as apparently the decrease in number of Earth pixels, and thus the decrease in resolution seen of the Earth's surface, seems to have had a stronger effect on the algorithm performance to overcome the gains seen from having higher signal-to-noise on each pixel.

While the cross-spectrum phase correlation method and optic flow algorithm performed well at the original 1 λ/D pixel resolution, their performance decreased as the pixels covered a wider field of view and thus the number of Earth pixels decreased. Neither algorithm was able to meet the accuracy requirements at the new pixel resolutions using 2 or 2.5 λ/D pixels. The optic flow had better overall maximum error, average errors, and percentage of errors meeting the accuracy requirement than the cross-spectrum phase correlation method at the 2 λ/D pixel resolution. Although the optic flow algorithm did not meet the accuracy requirement all the time, it did have low enough errors fairly consistently to give it a $\geq$75% rate of meeting the accuracy requirement, making it a fairly reasonable choice for this resolution if no other algorithms had performed better. At the 2.5 λ/D pixel resolution neither algorithm performed well enough to be considered should this resolution have been chosen, with both algorithms showing high overall maximum errors, high average errors, and a low percentage of the errors meeting the accuracy requirement.

The algorithms were not retested for their computational costs at the new resolutions because since the number of pixels being processed in each timeframe decreased, it was assumed that the execution time on the PowerPC microprocessor would also decrease. If the cross-spectrum phase correlation method had performed well at the 2 or 2.5 λ/D pixel resolutions, this decrease in computation time might have made it run at a sufficiently fast execution time to be considered for the MLCD mission. However, since for these new resolutions only the threshold-centroiding algorithm met the accuracy requirements, and since it was already found to run quickly enough even when more pixels had to be processed, no new computational cost evaluations were performed.

2 λ/D pixels were eventually chosen for the MLCD mission, and the thresholded-centroiding algorithm was chosen as the only algorithm that met the accuracy re-

quirement and computational cost constraint.

Chapter 4

Using the Earth as a Tracking Reference

Once the thresholded-centroid algorithm was chosen for the MLCD mission, questions arose about using the Earth as a tracking reference that required further analysis. The Earth's albedo varies across the Earth's surface at 1.06 μm, and this variation is not constant in time. During the testing and evaluation of all the algorithms, the Earth's surface in successive camera frames was kept constant over short periods of time, as it was assumed that the albedo variations in time would not be significant enough to affect the tracked Earth locations returned by each algorithm. This assumption is validated in this chapter by identifying the most significant sources of albedo variations in time and showing that their effects on the optical centroid over short periods of time are insignificant.

In addition, the spatial albedo variations across the Earth's surface raised questions about the relative locations of the center of brightness of the Earth image and the physical center of the Earth. Knowing the relationship between these two locations is important in the signal acquisition phase of the mission. Once the Earth's location has been determined, the beacon must be located on the Earth's surface. Information will be stored in memory on how to find the beacon using simple geometric calculations from the location of the Earth's physical center. Thus, knowing the difference between the optical and physical center of the Earth defines a search

area in which to look for the beacon signal. Images from NASA's Clementine mission data set [11] were again used to help answer this question, this time to see how adding spatial albedo variations on the Earth's surface moves the location of the geometric center to the optical centroid. In addition to image analysis, lab experiments were conducted using the focal plane array that will be used on the MLCD mission. An experiment was conducted to measure how much the optical centroid varies with different spatial albedo patterns on an Earth "source." By comparing these optical centroid locations with the geometric centroids given by a constant albedo pattern, the approximate size of the search area for the beacon during the mission could be determined.

4.1 Related Work

The Clementine mission images [11] were again used for this research, this time used to analyze the difference between the optical centroid and geometric center of the Earth-phase-angle disk.

Chen [4] previously investigated how uncertainties in knowledge of the spatial albedo distribution across the Earth's surface affect the accuracy of a tracking system that uses the sunlit Earth as a pointing reference. In this case, knowledge of the albedo distribution of the Earth was used to derive the location of the Earth's physical center, and from there the ground station receive terminal. The uncertainties in the spatial albedo distribution thus led to errors in pointing at the receive terminal. The MLCD system will use a blended beacon- and Earth-tracking system, where search is required to find the beacon in a small uncertainty area determined during acquisition by information gathered from the Earth-tracking system. During subsequent pointing and tracking, it is assumed (and verified in this chapter) that the Earth's albedo varies slowly enough that its distribution is known with good accuracy at the frequency at which the Earth-tracking system will be operating.

Lee *et al.* [10] studied the feasibility of using Earth images taken at wavelengths in the thermal infrared bands for pointing and tracking systems. Thermal images were

considered because of the relatively low amount of spatial variation of the Earth's surface albedo at these wavelengths. In addition, even the dark side of the Earth shows up in thermal images such that a full Earth disk is always seen, thus making the optical centroid line up more closely with the Earth's physical center, without additional geometric calculations to move a geometric Earth-phase-angle disk centroid to the physical Earth center. Earth images in the visible and near-infrared bands are dismissed due to the low signal strength at high phase angles (when the Earth is a small crescent), and the variations of the Earth's albedo in time. For the MLCD mission, however, the beacon will be strong enough to cover pointing and tracking operations during periods of high Earth phase angle, and the MLCD camera resolution will be low enough that the Earth's albedo variations in time will be less significant than in the higher resolution systems considered in this study. For other mission conditions and system designs, however, thermal images provide a plausible option for an Earth-tracking system.

4.2 Earth Albedo Variations Over Time

To analyze how the Earth's albedo variations in time affect the optical centroid, the most significant sources of these variations in time were identified and shown to be insignificant at the resolution and on the time scales we will be using on the MLCD mission. The albedo pattern on the Earth's surface seen from Mars will change due to the rotation of the Earth about its axis and due to weather patterns causing clouds to move across the Earth's surface. The fastest moving points on the Earth's surface due to rotation of the Earth about its axis lie along the equator and directly under the spacecraft, where the albedo patterns will change at 1667.88 km/hr. The fastest moving clouds, if the move at the speed of the jet streams, will move at 482.79 km/hr, almost 4 times slower than the fastest albedo changes due to the Earth's rotation about its axis. Rotation of the Earth is thus the most significant cause of albedo variations in time that will be seen by the Mars spacecraft camera, with the fastest changes occurring at 1667.88 km/hr.

Although in actuality only points along the equator and directly under the spacecraft will move at 1667.88 km/hr in the camera images, for simplicity it was shown that even if all points across the Earth's surface move at this speed, the effects on the optical centroid will still be insignificant. The entire Earth's surface translating at the Earth's rotation rate of 1667.88 km/hr is equivalent to a change of 0.0035% of the Earth's diameter in one second. This rate equates to a different number of pixels on the focal plane array depending on the day of the mission. Figure 4-1 shows the number of pixels covered by 0.0035% of the Earth's diameter throughout the mission. As can be seen in the figure, during the Earth-tracking phase of the mission from Day 160 - Day 808, 0.0035% of the Earth's diameter is at most 0.001 pixels in the worst case scenario. This is a very conservative estimate of the amount of movement that might be expected in the optical centroid due to albedo variations in time, 0.001 pixels per second. In one 4.8 ms timeframe, this will cause the centroid to move by at most $4.8 \cdot 10^{-6}$ pixels due to albedo variations, which is insignificant for the tracking performance of the centroiding algorithm.

4.3 Difference Between Optical and Physical Centroid

To analyze the difference between the optical and physical centroid, the optical centroid was compared to the geometric centroid of the sunlit Earth disk shape for 453 images of the Clementine data set. These images were taken over a 2-month period and show a range of Earth phase angles and spatial albedo variation patterns. A binary image of the Earth was generated for each Clementine image by setting a threshold to classify the Earth pixels as '1' and the background as '0'. Centroid calculations on these binary images yielded the geometric centroid of the sunlit Earth disk shape. Since the Earth phase angle is known for each Clementine image and will also be known at any time during the MLCD mission, geometric calculations can determine where the Earth's physical center is once the geometric centroid of

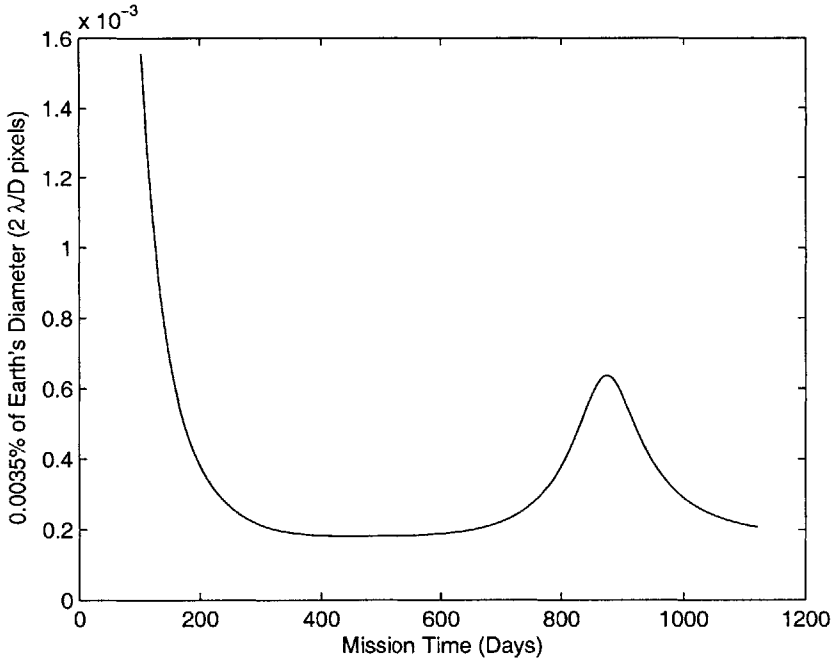

Figure 4-1: Number of pixels covering 0.0035% of the Earth's diameter versus mission time to indicate that albedo changes due to the Earth's rotation are a small fraction of a pixel in an FPA frame time

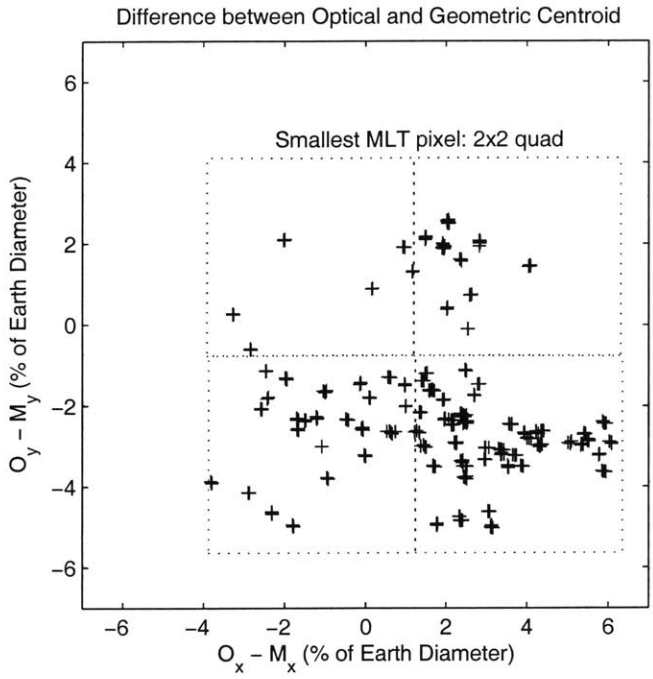

Figure 4-2: Difference between optical and geometric Earth centroids in Clementine images

the Earth shape has been located. The optical centroid of the Earth pixels is also calculated for each Clementine image, and the difference between the location of the optical and the geometric centroid was computed. The shifts between the locations of these two types of centroids are plotted for all 453 images in Figure 4-2.

Note that the difference between the optical and geometric centroids is given as a percentage of the Earth's diameter as opposed to in pixels. This is to allow for the difference to be scaled to pixels appropriately for any day of the MLCD mission, where the percentage of the Earth's surface covered by one pixel increases as the distance between Mars and Earth increases. At closest range, when the Earth spreads over 20 pixels in diameter, each pixel covers 5% of the Earth's diameter. As can be seen in the plots in Figure 4-2, this resolution moves the optical centroid from the geometric centroid by no more than 2 pixels at this point in the mission. As the range increases between the Earth and Mars, each pixel covers a greater percentage of the diameter and the optical centroid appears to move even less pixels from the geometric centroid.

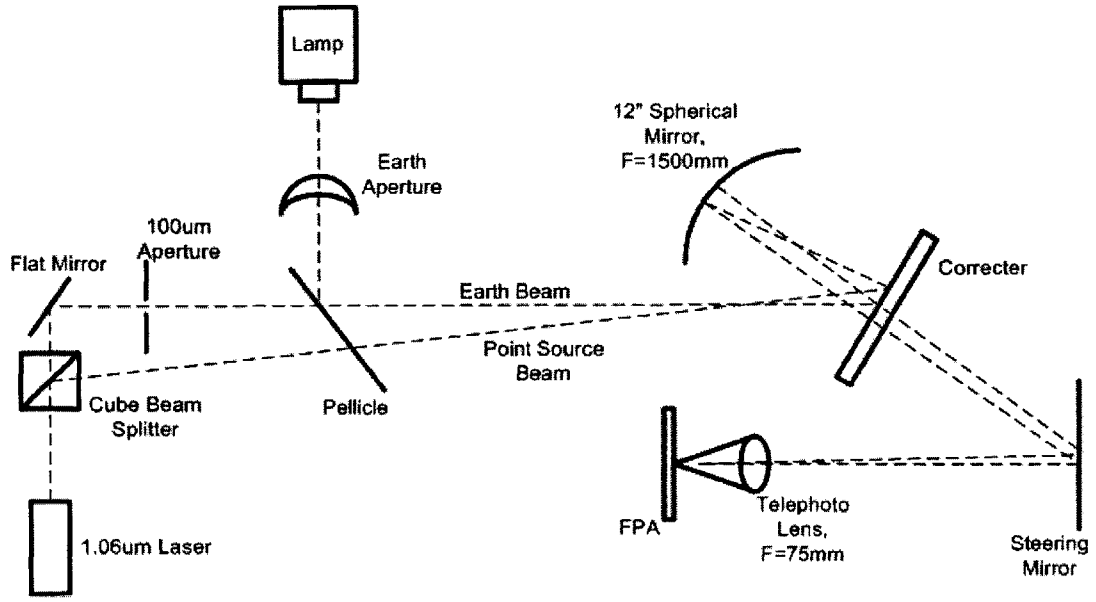

Figure 4-3: Optics test bench setup to simulate Earth and beacon images

Thus, the beacon search area should be roughly 2 pixels in radius at the closest range and can be a smaller area at further ranges.

This result was also verified in the lab using the actual focal plane array that will be used on the MLCD mission and the optics test bench setup as shown in Figure 4-3. The Earth source was generated by illuminating Clementine images (shown in Figure 4-4) placed over an aperture cut to match the shape and size of the Earth on the focal plane array for a given day of the mission. These Earth mask cutouts were generated for every 100 days on orbit, starting from the Mars Orbit Insertion date and continuing for two years. The Clementine images were printed on a film positive and placed over these Earth mask cutouts to properly attenuate the Earth signal through the aperture according to the albedo of each particular Earth surface area in the image.

The Earth was first imaged with no Clementine albedo image, so that the lamp light simply passed through the aperture to create a uniformly bright Earth disk on the focal plane array with no spatial albedo variations. The average centroid of several frames of this image gave the geometric centroid of the Earth for that

Figure 4-4: Clementine images used to simulate albedo variations on the Earth "source"

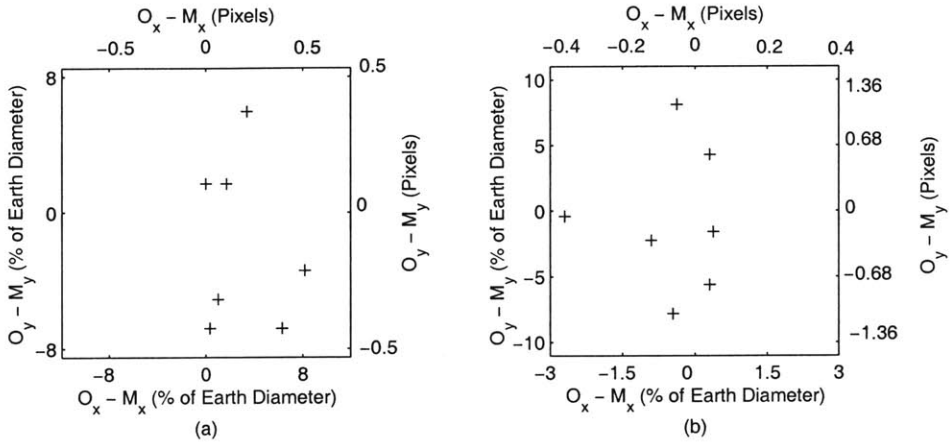

Figure 4-5: Experimental difference between optical and geometric centroid, in 2 λ/D pixels, for a) full Earth, and b) crescent Earth

particular mission day. A Clementine albedo image was then added on top of the Earth aperture to provide a spatially varying albedo, and the optical centroid of the resulting image was calculated for each albedo image placed over the aperture. This was done for two different apertures, a crescent Earth shape and a full Earth shape. The shifts in the location of the optical centroid from the geometric centroid are plotted for the different albedo images and Earth shapes in Figure 4-5, where each point in the plots represents the difference between the optical and geometric centroid in the x- and y-direction. As can be seen in the plots, having spatial albedo variations only moves the optical centroid from the geometric centroid by at most 2 MLCD pixels, the same result as obtained through Clementine image analysis.

Chapter 5

Summary

The Mars Laser Communication Demonstration (MLCD) project is a laser communication system that will demonstrate the capability of achieving 1-30 Mbps data rates from Mars using 1.06-μm laser communications during the Mars Telesat Orbiter (MTO) mission, achieving data rates that are 30 times higher than a comparable RF system. The MLCD system is currently in development for a 2009 launch and 3-year lifetime. Such a laser communication system presents a variety of new design challenges, including the design of a pointing and tracking system to point the laser beam from Mars to the ground station with 0.35 μrad accuracy, 10% of the beamwidth. Data from a variety of sensors on board the spacecraft will be used to help point the beam, including an Earth-tracking system to stabilize the beam from line-of-sight (LOS) jitter in the frequency range of 0.02 to 2 Hz. This thesis concerns the design of a computationally efficient Earth-tracking system that meets the 0.35-μrad (or 0.089-diffraction-limited pixel) accuracy requirement in the 0.02 to 2 Hz frequency disturbance range and runs in the allotted time frame of 4.8 ms.

Before testing candidate Earth-tracking algorithms, a simulation of Earth images that would be seen by the Mars camera during the MLCD mission was created to provide test data for the algorithms as no image test set previously existed. This simulation modeled several aspects leading up to the creation of images on the focal plane array, including: the orbital dynamics of the Earth, Sun, and spacecraft, the Earth's spatially-varying albedo and expected signal strength, the MTO's optics

subsystem, the LOS jitter expected during the mission, and the characteristics of the focal plane array. Further work on the simulation could also include the effects of the Earth's terminator, albedo variations in time, angular jitter due to rotation of the spacecraft, and non-uniformity of the pixels in the FPA, all of which are second-order effects that are expected to be insignificant. Although this simulation was used to create images specific to the parameters of the MLCD mission, the steps followed in the generation of the Earth images can be used to make simulated images for other deep-space pointing and tracking problems by altering the appropriate parameters.

After testing the plain-centroid algorithm, thresholded-centroid algorithm, cross-spectrum phase correlation method, and optic flow algorithm, the centroiding algorithm that tracked the centroid of the thresholded Earth pixels was chosen as the only algorithm to meet the accuracy and computational cost requirements for the MLCD mission. Although the thresholded-centroiding algorithm was chosen for this mission, it might not be the best algorithm under other conditions. As discussed in Chapter 3, the cross-spectrum phase correlation and optic flow algorithms also met the accuracy requirement when diffraction-limited pixels were used. If given the computational resources, these algorithms could also be used at this resolution in place of the thresholded-centroiding algorithm, particularly if the background conditions are not as favorable as in the MLCD mission such that the Earth cannot be segmented by thresholding alone. The cross-spectrum phase correlation and optic flow algorithms are also more robust to noise, giving them a greater potential to achieve high accuracy than the thresholded-centroid algorithm in higher noise conditions. In addition, with even greater pixel resolution, more detail will be seen in the Earth's surface albedo, making the effects of the time-varying albedo more apparent. If the images can no longer be expected to be simple shifted versions of each other from frame-to-frame, the algorithms tested for the MLCD mission may no longer be appropriate.

Finally, once the thresholded-centroid algorithm was chosen, the Earth's varying albedo was analyzed to determine its effects on the Earth-tracking system. For the conditions of the MLCD mission, 1-μm Earth images from the Clementine mission were tested as an absolute pointing reference to understand the effects of the Earth's

varying surface albedo. The most significant effect on the Earth centroid under MLCD conditions from short-term albedo variations was shown to be limited by the Earth's rotation, and thus too slow to change the Earth's surface enough to affect the centroid calculation between time frames. Differences between the geometric centroid and optical centroid were measured to be up to 10% of the Earth's diameter, or up to 2 focal plane array pixels during the mission at closest range. As such, the uncertainty area in which to search for the beacon is limited to a 2-pixel radius.

Bibliography

[1] A. Averbuch and Y. Keller. FFT based image registration. In *Proc. IEEE International Conference on Acoustics, Speech, and Signal Processing*, volume 4, pages 3608–3611, May 2002.

[2] A. Biswas and S. Piazzolla. Deep-space optical communications downlink budget from Mars: System parameters. IPN Progress Report 42-154, Jet Propulsion Laboratory, Pasadena, California, August 2003.

[3] P.J. Burt and E.H. Adelson. The Laplacian pyramid as a compact image code. *IEEE Trans. on Communications*, COM-31(4):532–540, April 1983.

[4] C.-C. Chen. Effect of Earth albedo variation on the performance of a spatial acquisition subsystem aboard a planetary spacecraft. The Telecommunications and Data Acquisition Progress Report 42-95, July-September, Jet Propulsion Laboratory, Pasadena, California, November 1988.

[5] H. Hemmati. Free-space optical communications at JPL and NASA. Review paper, Jet Propulsion Laboratory, Pasadena, California, March 2003.

[6] H. Hemmati, K. Wilson, M.K. Sue, L.J. Harcke, M. Wilhelm, C.-C. Chen, J. Lesh, and Y. Feria. Comparative study of optical and radio frequency communication systems for a deep-space mission. TDA Progress Report 42-128, Jet Propulsion Laboratory, Pasadena, California, February 1997.

[7] B.K.P. Horn and B.G. Schunck. Determining optical flow. Memo 572, M.I.T. Artificial Intelligence Laboratory, Cambridge, Massachusetts, April 1980.

[8] C.D. Edwards Jr., C.T. Stelzried, L.J. Deutsch, and L. Swanson. NASA's deep space telecommunications road map. TMO Progress Report 42-136, Jet Propulsion Laboratory, Pasadena, California, February 1999.

[9] S.G. Lambert and W.L. Casey. *Laser Communications in Space.* Artech House, Inc., 1995.

[10] S. Lee, G.G. Ortiz, W.T. Roberts, and J.W. Alexander. Feasibility study on acquisition, tracking, and pointing using Earth thermal images for deep-space Ka-band and optical communications. IPN Progress Report 42-155, Jet Propulsion Laboratory, Pasadena, California, November 2003.

[11] NASA/JPL-Caltech. NASA Planetary Image Atlas: Clementine mission. http://pds-imaging.jpl.nasa.gov/cgi-bin/Clem/jpl_clsearch.pl, 2004-2005.

[12] N. Otsu. A threshold selection method from grey-level histograms. *IEEE Trans. on Systems, Man, and Cybernetics*, 9(1):62–66, January 1979.

[13] H.S. Stone, M.T. Orchard, F.-C. Chang, and S.A. Martucci. A fast direct Fourier-based algorithm for subpixel registration of images. *IEEE Trans. on Geoscience and Remote Sensing*, 39(10):2235–2243, October 2001.

[14] G.H. Suits. *Natural Sources: The Earth as Seen from Space - Albedo*, section 3.5.1. The Infrared Handbook. Office of Naval Research, Dept. of the Navy, Arlington, Virginia, revised edition, 1985.